ALMA MATER STUDIORUM · UNIVERSITÀ DI BOLOGNA

Scuola di Scienze
Corso di Laurea Magistrale in Fisica del Sistema Terra

IMPACT OF WATERBODY EVAPORATION IN AN URBAN CANYON INVESTIGATED THROUGH LARGE-EDDY SIMULATIONS

Relatrice:
Prof.ssa Silvana Di Sabatino

Correlatore:
Dott. Carlo Cintolesi

Presentata da:
Marco Pancaldi

Sessione III
Anno Accademico 2020/2021

Abstract

Lo studio dell'evaporazione da parte di specchi d'acqua in ambiente urbano può contribuire alla comprensione dei fenomeni micrometeorologici e allo sviluppo di soluzioni per migliorare il comfort delle città. Questo problema è stato affrontato usando una simulazione fluidodinamica di un canyon urbano al cui centro è stato posto un canale d'acqua. Per le simulazioni è stato usato un modello di fluidodinamica computazionale sviluppato usando OpenFOAM. Come approccio numerico è stata usata una large-eddy simulation. Tale approccio ha permesso di simulare l'evoluzione del sistema e di analizzarne le variabili medie e turbolente. Il modello è basato su un solutore fluidodinamico in approssimazione di Boussinesq a cui sono state aggiunte le equazioni di avvezione diffusione del vapore e lo scambio termico provocato dall'evaporazione. Inoltre sono state implementate delle condizioni al contorno che potessero modellizzare l'evaporazione d'acqua dal canale. Il modello è stato validato simulando un canale piano usando diversi modelli di turbolenza. Sono state eseguite due simulazioni del canyon urbano, una prima in cui il canale ha una temperatura maggiore dell'aria circostante, e una seconda in cui la temperatura del canale è inferiore all'aria. In entrambe le simulazioni la presenza del canale ha influenzato fortemente sia le variabili medie che turbolente. L'evaporazione d'acqua dal canale e il conseguente galleggiamento ha portato un aumento dell'intensità della velocità all'interno del canyon. Si è assistito inoltre ad un abbassamento delle temperature su tutto il dominio, in particolare nel caso col canale freddo, all'interno del canyon, si è raggiunto un raffreddamento del 10-20% rispetto alla differenza di temperatura tra il canale e la temperatura ambientale iniziale. Si è inoltre osservato un aumento dell'energia cinetica turbolenta in tutto il dominio, e un aumento di flussi turbolenti di quantità di moto soprattutto all'interfaccia tra il canyon e l'aria esterna.

Abstract

The study on waterbodies evaporation in an urban environment can contribute to the understanding of micrometeorological phenomena and the development of solutions to improve the urban comfort. This problem was addressed using a fluid dynamics simulation of an urban canyon with a water channel in the middle. A computational fluid dynamics (CFD) model developed using OpenFOAM was used for the simulations. For the numerical approach, a large-eddy simulation (LES) was used. This approach made it possible to simulate the evolution of the system and to analyse its mean and turbulent variables. The model is based on a fluid dynamics solver in the Boussinesq approximation, to which the equations of vapor advection-diffusion and heat transfer caused by evaporation have been implemented. In addition, boundary conditions were implemented to model the evaporation of water from the channel. The model was validated by simulating a flat channel using different turbulence models. Two simulations of the urban canyon were performed, a first one in which the channel has a higher temperature than the surrounding air, and a second one in which the temperature of the channel is lower than the air. In both simulations the presence of the channel strongly influenced both the mean and turbulent variables. The evaporation of water from the channel and the resulting buoyancy led to an increase in the velocity intensity within the canyon. There was also a lowering of temperatures over the entire domain, in particular in the case of the cold channel, inside the canyon, a 10-20% cooling was achieved regarding the temperature difference between the channel and the initial ambient temperature. An increase in turbulent kinetic energy was also observed throughout the domain, and an increase in turbulent momentum fluxes was observed especially at the interface between the canyon and the outside air.

Contents

Introduction

Nowadays, more than half of the human population lives in urban areas and the percentage is estimatedto rise to 68% by 2050, acording to the world urbanization prospect of the United Nations [3]. It is well known that urban temperature is usually warmer than surrounding rural areas, this phenomenon is called urban heat island (UHI). The causes of UHI are several from the street geometry, to the presence of artificial surface with high emissivity, and the presence of anthropogenic heat source. Climate change is expected to worsen the situation with higher temperatures and more frequent and intense heatwaves. there is a wide litterature on possible solutions to improve urban comfort [25] to reduce morbidity and mortality in urban settlements. An important ensemble of strategies to mitigate the UHI are the natural-based solutions (NBS) that are inspired by, supported by or copied from nature, including for example threes and water basins in the urban texture. To insert water bodies may reduce the temperature due to the evaporation, but may also increase the urban humidity and changes the dynamics producing a buoyancy effect. Understanding the behaviour of evaporation in urban areas and the dynamics of moisture is important to gain knowledge about the impact of the existing water bodies and to predict the consequences of the implementation of water basins in the urban planning of the new neighbourhood.

Some articles were published, which adress the problem from different points of view, using numerical modelling, field measures, laboratory experiments and scale models. Hathway et al. [10] have studied the impact of an urban river in England using field measures and showing a cooling effect of 1.5 °C during the spring period. This effect is smaller during the summer season due to the high water temperature. Theeuwes et al. [23] have studied a simulation of a circular city surrounded by a rural area performed with the weather research and forecasting (WRF) model. Inside the city they have set some water basins of different sizes and forms. They found that greater lakes produce greater impact but only near the edge and in the downwind area, instead of many small lakes producing smaller impact but involving greater areas. They also noticed that during the night the water temperature may be higher than the air temperature heating the environment. Tominaga et al. [24] used a model which combine a Reynolds-averaged Navier-Stokes equations (RANS) simulation and a radiative model. After the validation of the model using a model of buildings array and a river in a wind tunnel, they have

simulated a residential area in Japan that contain a pound, and they compared the simulation with the field measurements. They found a maximum temperature decrease of $2\,^{\circ}C$ at the pedestrian level, with an extension of 100 m with a wind of 10 m/s at 3 m high. Montazeri et al. [15] studied the effect of a water spray used in a courtyard in the Netherlands during a heatwave in 2006, using a RANS simulation comparing it with fields and satellite measurements, obtaining a temperature reduction of about 7 and $5\,^{\circ}C$ at pedestrian level. Since the 1970s one of the most important research topics in the context of urban micrometeorology is the study of street canyons [18, 17]. Pearlmutter et al. [19] have created a scale model of an array of street canyons with evaporation pans that simulate vegetative areas to study the evapotranspiration impact. Syafii et al. [11] have created a scale model of buildings array with some water pounds in different positions and of different forms. They found better thermal environments in presence of the pounds, but also an increase in absolute humidity which may worsen the pedestrian comfort. They also founded a more efficient cooling effect with pounds oriented parallel to prevailing winds. Kubilay et al. [13] worked on a RANS simulation of a street canyon in which water evaporates from the surfaces of buildings which are wet from the rain. They found that the increase in the rainfall intensity does not change the reduction in surface temperature, but extends the duration of the cooling effect. They also have studied the impact of materials founding that the moisture permeability, moisture capacity and thermal diffusivity, affected the thermal comfort. Zhao et al. [27] in their review point out that, for the study of street canyon dynamics, it would be better to use models that take into account the temporal evolution such as large-eddy simulations (LES) and unsteady RANS (URANS) simulations instead of the more used RANS. However, dealing with the phase change of water in a fluid dynamic simulation is not a simple thing because turbulent flows with a high Reynolds number, are complex nonlinear systems. Today no a LES is treating the evaporation and the moisture role in a street canyon.

Cintolesi et al. [6] proposed a model to simulate the evaporation from a water film in a turbulent flow using a LES. In the present work, such an evaporation model is applied to an urban street canyon with an evaporating waterbody. This allows the investigation of effects of evaporation and vapour concentration in the air circulation. Two different simulation are performed with different temperature of the water to simulate a diurnal configuration with the waterbody colder than the air, and a nocturnal configuration with the waterbody warmer than the air. The model is implemented using the software toolbox OpenFOAM [26, 2, 1], which is a computational fluid dynamic open source software written in C++. It is used the OpenFOAM solver buoyantBoussinesqPimpleFoam, which simulate the motion of a fluid in Boussinesq approximation with buoyancy due to temperature and humidity change. That solver is changed to simulate the evaporation from the waterbody and to take into account the vapour concentration diffusion and buoyancy contribution.

The first chapter will show the mathematical models used to model the dynamic of

the system and the evaporation, and the numerical approaches used to model turbulence. In the second chapter, the numerical implementation of the mathematical models will be shown with particular attention to the boundary conditions used to simulate the evaporation of the water film. In the third chapter, the model will be validated using the archetype case of channel flow which is well known and studied in depth [16]. Three different turbulence models have been used the Smagorinsky, the wall adapting local eddy-viscosity model (WALE) [9] and the dynamic Lagrangian [14]. Wall functions proposed by desoutter et al. [8] will be used to validate the evaporation model. The fourth chapter will be shown the analysis of the simulations made on the street canyon and the results obtained. Finally, in the fifth chapter, the conclusions drawn from this work are reported.

Chapter 1

Theoretical models

1.1 Mathematical models

1.1.1 Navier-Stokes equations

The motion of a fluid is described by the Navier-Stokes equations, which is a system of equations including the conservation of mass and the conservation of momentum. According to the Boussinesque approximation, the variation of density will be neglected except in the gravitational term.

For an incompressible fluid, the equation of mass conservation is:

$$\frac{\partial u_i}{\partial x_i} = 0 \tag{1.1}$$

where u is the fluid velocity, and x is the cartesian coordinate.

The momentum conservation equation is:

$$\frac{\partial u_i}{\partial t} + u_j \frac{\partial u_i}{\partial x_j} = -\frac{1}{\rho_0}\frac{\partial p}{\partial x_i} + \nu \frac{\partial^2 u_i}{\partial x_j \partial x_j} - \frac{\rho}{\rho_0} g \delta_{i3} \tag{1.2}$$

where t is the time, ρ_0 is the reference density, p is the pressure, ν is the kinematic viscosity, ρ is the density and g is the gravitational acceleration.

The vapour concentration ω is Defined as the ratio between the mass of vapour m_v and the sum of the masses of vapour and dry air m_a:

$$\omega = \frac{m_v}{m_a + m_v}. \tag{1.3}$$

The density ρ is supposed to be a linear function of the temperature T and the vapour concentration:

$$\frac{\rho}{\rho_0} = 1 - \beta_T(T - T_0) - \beta_\omega(\omega - \omega_0) \tag{1.4}$$

where β_T and β_ω are respectively the expansion coefficients for the temperature and vapour concentration.

The density depends on both T and ω which are active scalar, and are diffused and transported following the advection-diffusion equation:

$$\frac{\partial T}{\partial t} + u_j \frac{\partial T}{\partial x_j} = \alpha_T \frac{\partial^2 T}{\partial x_j \partial x_j} + S \tag{1.5}$$

$$\frac{\partial \omega}{\partial t} + u_j \frac{\partial \omega}{\partial x_j} = \alpha_\omega \frac{\partial^2 \omega}{\partial x_j \partial x_j} \tag{1.6}$$

where α_T and α_ω are the coefficients of diffusion for T and ω, and S is a source term due to the energy exchange produced by evaporation as explained in the next section.

1.1.2 Evaporation model

To describe the evaporation of water, is used a mathematical model yet used in other research [6, 7, 20]. The waterbody is modelled as an evaporating film with constant physical properties. The only property of the water film that changes in time is the height.The model considers only the evaporation and condensation which take place in the boundary in contact with the water film.

Using the molar masses M and the number of moles n for vapour (subscript v) and dry air (subscript a), it is possible to express omega as a function of atmospheric pressure p_{atm} and vapour pressure e

$$\omega = \frac{m_v}{m_a + m_v} = \frac{M_v n_v}{M_a n_a + M_v n_v} = \frac{M_v n_v}{M_a n_a}\left(\frac{1}{1 + \frac{M_v n_v}{M_a n_a}}\right)$$

$$= \frac{M_v}{M_a}\left(\frac{e}{p_{atm} - e}\right)\left(\frac{1}{1 + \frac{M_v}{M_a}\frac{e}{p_{atm} - e}}\right) = \frac{M_v}{M_a}\left(\frac{e}{(p_{atm} - e) + \frac{M_v}{M_a}e}\right). \tag{1.7}$$

The vapour pressure may be replaced by the vapour pressure at saturation multiplied for the relative humidity. Assuming that in contact with the water film the water is saturated is possible to compute the value of the concentration of vapour at the interface

$$\omega_\Gamma = \frac{M_v}{M_a}\left(\frac{e_s}{p_{atm} - (1 - \frac{M_v}{M_a})e_s}\right). \tag{1.8}$$

The saturation pressure (e_s) is computed using the Buck's equation

$$e_s(T_\Gamma) = 611.85 \, exp\left(\frac{17.502 T_\Gamma}{240.9 + T_\Gamma}\right). \tag{1.9}$$

The velocity of evaporation may be estimated by Fick's law for the diffusion of vapour. Since ω includes both the mass of vapour and air it is necessary to divide the diffusion flow of omega by the mass of dry air $(1 - \omega_\Gamma)$

$$\mathbf{U}_\omega = -\frac{\alpha_\omega}{1 - \omega_\Gamma} \left(\frac{d\omega}{dn}\bigg|_\Gamma \right) \hat{n}. \tag{1.10}$$

From U_ω is computed the heat flux vector:

$$\mathbf{q} = \rho^* L_h \mathbf{U}_\omega. \tag{1.11}$$

where ρ^* is the sum of the density of air and water, and L_h is the latent heat of vaporization, both are considered constant. The divergence of $\mathbf{q}$ represents the energy stored in an air particle near the water film, dividing it by heat capacity is possible to compute the source term in the temperature equation (1.5):

$$S = -\frac{1}{\rho\, C_p} \nabla \cdot \mathbf{q}. \tag{1.12}$$

Evaporation, therefore, behaves like a temperature sink that acts on the cells adjacent to the boundary with the water film.

The evolution of the height (H) of the water film is computing using U_ω

$$\frac{\partial H}{\partial t} = \frac{\rho_a}{\rho_w} \mathbf{U}_\omega \tag{1.13}$$

where ρ_a is the density of the air and ρ_w is the density of water, while $\rho_a/\rho_w = 0.001$, following Ref. [20].

1.2 Large-eddy simulation

In order to resolve the Navier-Stokes equation, in a finite computational grid, a spatial filter has been apply. The spatial filter is defined by a filtering operation:

$$\overline{\mathbf{u}}(\mathbf{x}, t) = \int \mathbf{G}(\mathbf{r}, \mathbf{x}) \mathbf{u}(\mathbf{x} - \mathbf{r}, t) d\mathbf{r}$$

where $\mathbf{G}$ is a filter function.

The momentum conservation equation becomes:

$$\frac{\partial \overline{u}_i}{\partial t} + \frac{\partial \overline{u_j u_i}}{\partial x_j} = -\frac{1}{\rho} \frac{\partial \overline{p}}{\partial x_i} + \nu \frac{\partial^2 \overline{u}_i}{\partial x_j \partial x_j}. \tag{1.14}$$

The equation depends both on $\overline{u}_i$ and $\overline{u_i u_j}$ so the system is not closed. Introducing the residual stress tensor:

$$\tau_{ij}^R = \overline{u_i u_j} - \overline{u}_i \overline{u}_j$$

which may be divided into an anisotropic and an isotropic part:

$$\tau_{ij}^R = \tau_{ij}^r + \frac{2}{3} k_r \delta_{ij}.$$

The isotropic part may be included in the pressure therm, so the equation (1.14) becomes

$$\frac{\partial \overline{u}_i}{\partial t} + \frac{\partial \overline{u}_j \overline{u}_i}{\partial x_j} = -\frac{1}{\rho} \frac{\partial \overline{p}}{\partial x_i} + \nu \frac{\partial^2 \overline{u}_i}{\partial x_j \partial x_j} - \frac{\partial \tau_{ij}^r}{\partial x_i}.$$

Than modelling τ_{ij}^r the problem may be closed. different modelization of τ_{ij}^r exist, in this work there will be used the Smagorinsky, the WALE and the dynamic Lagrangian. These three turbulence models will be explained in the next section.

1.3 Turbulence models

1.3.1 Smagorinsky model

The Smagorinsky model is based on the hypothesis that the subgrid-scale (sgs) shear stress is linearly related to the resolved rate of the strain tensor.

$$\tau_{ij}^{sgs} = -2\nu_{sgs} \overline{S}_{ij} \tag{1.15}$$

This hypothesis is known as the linear eddy-viscosity model and treats the effect of turbulence in the subgrid-scale as a viscosity acting on the grater scale motion. The eddy viscosity of the residual motion ν_{sgs} is computed using the mixing length hypothesis

$$\nu_{sgs} = l_s^2 \left| \overline{S} \right| \tag{1.16}$$

where l_s is the Smagorinsky mixing-length

$$l_s = (C_s \Delta) \tag{1.17}$$

where Δ is the linear dimension of the cell, and C_s is the Smagorinsky constant. So ν_{sgs} becomes

$$\nu_{sgs} = (C_s \Delta)^2 \left| \overline{S} \right| \tag{1.18}$$

The OpenFOAM implementation of the Smagorinsky model, used in this work, is a bit more complex and will be explained in the following. It starts dividing the SGS stress tensor (τ_{ij}) into an isotropic and an anisotropic part

$$\tau_{ij} = \frac{1}{3} \tau_{kk} \delta_{ij} + \left(\tau_{ij} - \frac{1}{3} \tau_{kk} \delta_{ij} \right) \tag{1.19}$$

9

The isotropic part is proportional to the SGS kinetic energy (k_{sgs}) while the anisotropic part is assumed to behave as a viscosity proportional to the resolved rate of strain tensor $(\overline{D}_{ij})$ following the eddy viscosity approximation.

$$\tau_{ij} = \frac{2}{3}k_{sgs}\delta_{ij} - 2\nu_{sgs}\,dev\left(\overline{S}\right)_{ij} \tag{1.20}$$

where ν_{sgs} is the SGS viscosity, computed as

$$\nu_{sgs} = C_k\Delta\sqrt{k_{sgs}} \tag{1.21}$$

where C_k is a constant. k_{sgs} is computed assuming that the subgrid-scale are in local equilibrium so the energy production is in balance with the dissipation

$$\overline{S}_{ij}\tau_{ij} + C_\epsilon\frac{k_{sgs}^{1.5}}{\Delta} = 0 \tag{1.22}$$

Solving that equation using the definition of ν_{sgs}

$$\overline{S}_{ij}\left(\frac{2}{3}k_{sgs}I - 2\nu_{sgs}\,dev\left(\overline{S}\right)\right)_{ij} + C_\epsilon\frac{k_{sgs}^{3/2}}{\Delta} = 0$$

$$\overline{S}_{ij}\left(\frac{2}{3}k_{sgs}I - 2C_k\Delta\sqrt{k_{sgs}}\,dev\left(\overline{S}\right)\right)_{ij} + C_\epsilon\frac{k_{sgs}^{3/2}}{\Delta} = 0 \tag{1.23}$$

$$\sqrt{k_{sgs}}\left(\frac{C_\epsilon}{\Delta}k_{sgs} + \frac{2}{3}tr\left(\overline{S}\right)\sqrt{k_sgs} - 2C_k\Delta\left(dev\left(\overline{S}\right)_{ij}\overline{S}_{ij}\right)\right) = 0$$

The last equation may be rewritten as

$$ak_{sgs} + b\sqrt{k_{sgs}} - c = 0 \tag{1.24}$$

where a, b and c are defined as

$$a = \frac{C_\epsilon}{\Delta}$$
$$b = \frac{2}{3}tr\left(\overline{S}\right) \tag{1.25}$$
$$c = 2C_k\Delta\left(dev\left(\overline{S}\right)_{ij}\overline{S}_{ij}\right)$$

So the equation (1.24) has the solution

$$k_{sgs} = \left(\frac{-b + \sqrt{b^2 + 4ac}}{2a}\right)^2 \tag{1.26}$$

for an incompressible fluid, $\overline{S}$ is traceless so $dev(\overline{S}) = \overline{S}$ and

$$b = 0$$
$$c = C_k \Delta |\overline{S}|^2 \tag{1.27}$$

so k_{sgs} and ν_{sgs} become

$$k_{sgs} = \frac{C_k \Delta^2 |\overline{S}|^2}{C_\epsilon}$$
$$\nu_{sgs} = C_k \sqrt{\frac{C_k}{C_\epsilon}} \Delta^2 |\overline{S}| \tag{1.28}$$

wich is equal to the equation (1.18) where

$$C_s^2 = C_k \sqrt{\frac{C_k}{C_\epsilon}}. \tag{1.29}$$

Using cells of different shapes and sizes, the linear dimension Δ of each cell is computed as the cube root of the volume.

In real turbulent flows, near a wall, a viscous sublayer forms. In this sublayer, the viscous forces dominate over the inertial ones producing a laminar boundary layer, and the turbulence viscosity should go to zero near the wall. But in the Smagorinsky model, the large velocity gradients produce a value of $\overline{S}_{ij}$ and therefore of ν_{sgs} different from zero. It is, therefore, necessary to introduce a correction to l_s so that it goes to zero as it approaches the wall:

$$l_s = C_s \Delta f(z^+) \tag{1.30}$$

where z^+ is the non-dimensional wall-normal coordinate, defined as

$$z^+ = \frac{u^* z}{\nu} \tag{1.31}$$

with ν viscosity, u_τ friction velocity and z wall-normal direction. In this work is used a Van Driest dumping function

$$f(z^+) = \sqrt{(1 - e^{-z^+/A})^3} \tag{1.32}$$

where A is an empirical constant set to 25.

1.3.2   Wall adapting local eddy-viscosity model

The wall adapting local eddy-viscosity model (WALE) was proposed by Nicoud and Ducros in 1999 [9] in order to improve the Smagorinsky model. It includes the contribution of the rotation rate to the subgrid-scale stress tensor, and the turbulent viscosity

goes to zero approaching the wall. As the Smagorinsky, the WALE model assumes that the SGS turbulent viscosity is proportional to the square root of the SGS turbulent kinetik energy:

$$\nu_{sgs} = C_k \Delta \sqrt{k_{sgs}} \tag{1.33}$$

but as invariable to compute the subgrid turbulent kinetic energy is used the traceless symmetric part of the square of the velocity gradient

$$S_{ij}^d = \frac{1}{2} \left(\frac{\partial \overline{u}_k}{\partial x_i} \frac{\partial \overline{u}_j}{\partial x_k} + \frac{\partial \overline{u}_k}{\partial x_j} \frac{\partial \overline{u}_i}{\partial x_k} \right) - \frac{1}{3} \delta_{ij} \frac{\partial \overline{u}_k}{\partial x_l} \frac{\partial \overline{u}_l}{\partial x_k} \tag{1.34}$$

k_{sgs} is then computed from S_{ij}^d and $\overline{S}_{ij}$ as

$$k_{sgs} = \left(\frac{C_w^2 \Delta}{C_k} \right)^2 \frac{\left(S_{ij}^d S_{ij}^d \right)^3}{\left(\left(\overline{S}_{ij} \overline{S}_{ij} \right)^{5/2} + \left(S_{ij}^d S_{ij}^d \right)^{5/4} \right)^2}. \tag{1.35}$$

Finally, the subgrid turbulent viscosity becomes

$$\nu_{sgs} = (C_w \Delta)^2 \frac{\left(S_{ij}^d S_{ij}^d \right)^{3/2}}{\left(\overline{S}_{ij} \overline{S}_{ij} \right)^{5/2} + \left(S_{ij}^d S_{ij}^d \right)^{5/4}}. \tag{1.36}$$

It is possible to show [9] that approaching a wall, $\left(S_{ij}^d S_{ij}^d \right)^{3/2}$ behaves like d^3 (where d is the distance from the wall) and therefore approaches zero. This means that this model does not need a damping function near the walls.

1.3.3 Dynamic Lagrangian model

Another turbulence model for large-eddy simulations was proposed by Meneveau et al. in 1994 [14]. It is called dynamic Lagrangian and is based on the Smagorinsky model with the difference that C_s is non an empirical parameter but is computed during the simulation using information from the resolved scales. Taking into account a grid with cells size double than that used in the simulation, $\widehat{\Delta} = 2\Delta$ is possible to apply a spatial filter based on this grid. It is introduced L_{ij} which is the difference between the stress tensor of the two scales

$$T_{ij} - \widehat{\tau}_{ij} = \widehat{\overline{u}_i \overline{u}_j} - \widehat{\overline{u}}_i \widehat{\overline{u}}_j \equiv L_{ij}. \tag{1.37}$$

That difference may be estimated using the Smagorinsky model

$$T_{ij} - \widehat{\tau}_{ij} \simeq C_s 2\Delta^2 \left(\widehat{|\overline{S}| \overline{S}_{ij}} - 4|\widehat{\overline{S}}| \widehat{\overline{S}}_{ij} \right) \equiv C_s M_{ij} \tag{1.38}$$

The error between the two previous approaches is

$$e_{ij} = L_{ij} - C_s M_{ij} \tag{1.39}$$

The error in function of C_s is minimised in a last-square sense, along the particle trajectories covered in a time T:

$$\frac{\partial}{\partial C_s} \int_{-\infty}^{t} e_{ij}(x,t')e_{ij}(x,t')\frac{1}{T}e^{\frac{-(t-t')}{T}}dt' = 0. \tag{1.40}$$

Replacing e_{ij} with equation (1.39), and resolving in C_s it becomes

$$C_s = \frac{I_{LM}}{I_{MM}} \tag{1.41}$$

where I_{LM} and I_{MM} are defined as

$$I_{LM} = \int_{-\infty}^{t} L_{ij}M_{ij}\frac{1}{T}e^{\frac{-(t-t')}{T}}dt', \tag{1.42}$$

$$I_{MM} = \int_{-\infty}^{t} M_{ij}M_{ij}\frac{1}{T}e^{\frac{-(t-t')}{T}}dt'. \tag{1.43}$$

It is possible to show that I_{LM} and I_{MM} are solutions of the following equations

$$\frac{\partial I_{LM}}{\partial t} + \overline{\mathbf{u}}\nabla I_{LM} = \frac{1}{T}(L_{ij}M_{ij} - I_{LM}), \tag{1.44}$$

$$\frac{\partial I_{MM}}{\partial t} + \overline{\mathbf{u}}\nabla I_{MM} = \frac{1}{T}(M_{ij}M_{ij} - I_{MM}), \tag{1.45}$$

using as characteristic time

$$T = 1.5\Delta(I_{LM}I_{MM})^{-1/8}. \tag{1.46}$$

This is, generally, a more accurate model than the Smagorinsky but need more computational time because it resolves two auxiliary fields I_{LM} and I_{MM}.

Chapter 2

Numerical implementation

2.1 Solver description

The mathematical models described in the previous chapter, are implemented using the software toolbox OpenFOAM 6 from The OpenFOAM Foundation [26, 2, 1]. The OpenFOAM's solver buoyantBoussinesqPimpleFoam is used to resolve the equations of motion. It use uses the Boussinesq approximation, taking into account the contribution of buoyancy due to the thermal variation.

The solver has been modified to take into account the ω equation (1.6), its contribution in the buoyancy, and the evaporation model. The evaporation model was previously [6, 7, 20] written for a different solver (coupledHeatVapourFoam) on a different OpenFOAM version (v2.1). The files which described the evaporation model are rewritten in order to be compatible with the solver used and implemented in it.

The solver thus obtained was called humidityBuoyantBoussinesquePimpleFoam.

2.1.1 PISO algorithm

The pressure implicit with splitting of operators (PISO) algorithm proposed by Issa [12] is used in this work . From the discretization of equation (1.2) is computed the predicted values of velocity $\mathbf{u}^*$ from the values of velocity, pressure and density at the previous time steps $(\mathbf{u^n}, \mathbf{p^n}, \rho^\mathbf{n})$. The general form of this equation is:

$$\mathbf{C}\mathbf{u}^* = \mathbf{r} - \nabla\mathbf{p^n} + \rho^\mathbf{n}\mathbf{g} \tag{2.1}$$

where r is an explicit source term excluding pressure and buoyancy.

Then the first corrected velocity $(\mathbf{u}^{**})$ is computed from the following equation:

$$\mathbf{A}\mathbf{u}^{**} + \mathbf{H}'\mathbf{U}^* = \mathbf{r} - \nabla\mathbf{p}^* + \rho^\mathbf{n}\mathbf{g} \tag{2.2}$$

where $\mathbf{A}$ and $\mathbf{H}'$ are the diagonal and the off-diagonal parts of the matrix $\mathbf{C}$ ($\mathbf{C} = \mathbf{A} + \mathbf{H}'$), and $\mathbf{p}^*$ is the first corrected pressure which is still unknown. Since $\mathbf{A}$ is diagonal it

is simply invertible and the equation becomes

$$\mathbf{u}^{**} = \mathbf{A}^{-1}\mathbf{H} - \mathbf{A}^{-1}\nabla\mathbf{p}^* + \mathbf{A}^{-1}\rho^{\mathbf{n}}\mathbf{g} \qquad (2.3)$$

where $\mathbf{H}$ is $\mathbf{r} - \mathbf{H}'\mathbf{u}^*$. Knowing that for the continuity equation the velocity field must be solenoidal, is possible to find $\mathbf{p}^*$ imposing $\nabla\mathbf{u}^{**} = 0$.

$$\nabla^{\mathbf{2}}\left(\mathbf{A}^{-1}\mathbf{p}^*\right) = \nabla\left(\mathbf{A}^{-1}\mathbf{H} + \mathbf{A}^{-1}\rho^{\mathbf{n}}\mathbf{g}\right) \qquad (2.4)$$

from $\mathbf{p}^*$ is found $\mathbf{u}^{**}$ and using the same $\mathbf{A}$ and $\mathbf{H}$ is possible to repeat the last two equations to find the second and following corrector steps.

2.1.2 Solver structure

The main structure of the solver is the same as buoyantBoussinesqPimpleFoam with some additions because the original solver does not take into account the temperature source, the ω equation and the boundary condition to describe the evaporation.

For each cell, at each time step is defined the Courant number as:

$$Co = \frac{u\Delta t}{\Delta x} \qquad (2.5)$$

where u is the magnitude of the velocity, Δt is the time interval, and Δx is the cell linear dimension. Following the Courant convergence condition, there is a maximum value Co_{max} that can be reached to preserve system stability. At each time step, the solver computes Δt to have a max courant number Co_{max} of 0.5 using the scripts CourantNo.H and setDeltaT.H.

```
85      while (runTime.run())
86      {
87          #include "readTimeControls.H"
88          #include "CourantNo.H"
89          #include "setDeltaT.H"
90
91          runTime++;
92
93          Info<< "Time = " << runTime.timeName() << nl << endl;
```

Then the temperature (1.5) and humidity (1.6) equations and the evaporation model are resolved using the scripts TEqn.h and omegaEqn.H. TEqn.h and omegaEqn.H will be explained in detail in the following sections.

```
95          #include "TEqn.H"
96          #include "omegaEqn.H"
```

The PISO algorithm described in section 2.1.1 is implemented with the scripts UEqn.H and pEqn.H. The solver may be used with different turbulence models. After each step of the PISO loop, the turbulence parameters are updated.

```
101          // --- Pressure-velocity PIMPLE corrector loop
102
103          while (pimple.loop())
104          {
105              #include "UEqn.H"
106
107              // --- Pressure corrector loop
108              while (pimple.correct())
109              {
110                  #include "pEqn.H"
111              }
112
113              if (pimple.turbCorr())
114              {
115                  laminarTransport.correct();
116                  turbulence->correct();
117              }
118
119          }
```

At the end of the PISO loop, the temperature and humidity equations are recomputed to improve the coupling with the velocity and pressure equations.

```
121          #include "TEqn.H"
122          #include "omegaEqn.H"
123
124
125          runTime.write();
126
127          Info<< "ExecutionTime = " << runTime.elapsedCpuTime() << " s"
128              << "  ClockTime = " << runTime.elapsedClockTime() << " s"
129              << nl << endl;
130      }
```

In the next sections will be described TEqn.H and omegaEqn.H in detail.
UEqn.h and pEqn.H will not be treated in this work as they have not undergone significant changes compared to the original solver.

2.1.3 Temperature equation

At the start of the TEqn.H script, before resolving the temperature equation, the boundary fields are updated. The evaporation model are implemented through the function updateCoeffs(), the details of the function for each boundary are shown in subsequent sections.

```
157          forAll(omega.boundaryField(),b)
158              {
159                      omega.boundaryFieldRef()[b].updateCoeffs();
160              }
161
162
163          forAll(Uomega.boundaryField(),b)
164              {
165                      Uomega.boundaryFieldRef()[b].updateCoeffs();
166              }
167
168
```

```
169        forAll(EvCoHF.boundaryField(),b)
170                {
171                        EvCoHF.boundaryFieldRef()[b].updateCoeffs();
172                }
173
174
175        forAll(H.boundaryField(),b)
176                {
177                        H.boundaryFieldRef()[b].updateCoeffs();
178                }
```

following the Reynold analogy, the turbulent thermal diffusivity (alphat) is proportional to the turbulent viscosity (nut), and the proportional constant is the inverse of the turbulent Prandtl number (Prt).

```
184        alphat = turbulence->nut()/Prt;
185        alphat.correctBoundaryConditions();
```

The thermal diffusivity is computed using the Prandtl number and it is summed to the turbulent thermal diffusivity to obtain the efficient thermal diffusivity (alphaEff)

```
187        volScalarField alphaEff("alphaEff", turbulence->nu()/Pr + alphat);
```

The source term in eq. (1.5) is computed using the eq. (1.12) where the norm of **q** is implemented as a scalar field named EvCoHF. The computation of EvCoHF is described in detail in the section about his boundary condition.

```
189        surfaceScalarField EvCoSource ( fvc::interpolate(EvCoHF/(rho*Cp)) * mesh.magSf() );
```

Then is defined the matrix TEqn which describe the eq. (1.5)

```
191        fvScalarMatrix TEqn
192        (
193            fvm::ddt(T)
194          + fvm::div(phi, T)
195          - fvm::laplacian(alphaEff, T)
196         ==
197            radiation->ST(rhoCpRef, T)
198          + fvOptions(T)
199          + fvc::div(EvCoSource)
200        );
201
202        TEqn.relax();
203
204        fvOptions.constrain(TEqn);
205
206        TEqn.solve();
207
208        radiation->correct();
209
210        fvOptions.correct(T);
```

Finally, the equation (1.5) is resolved using the function solve() of the object TEqn.

2.1.4 Vapour concentration equation

The script which resolves the ω equation (1.6) is omegaEq.H. It is similar to TEq.H but there is no update of the boundary conditions of the evaporation model and the computing of the source therm, which is absent in eq (1.6). As the first thing, it is computed the turbulent diffusion, dividing the eddy viscosity to the turbulent Schmidt number. In the program the Schmidt number is called PrOmega for the formal similarity with the Prandtl number in the temperature diffusivity, as the other variable which as the name of the analogous in the TEqn.H adding Omega at the end.

```
157    alphaOmegat = turbulence->nut()/PrOmegat;
158    alphaOmegat.correctBoundaryConditions();
159
160    alphaOmegaEff = turbulence->nu()/PrOmega + alphaOmegat;
```

Is creating the object omegaEqn which is a matrix created using the discretization schemes for the differential operators. The equation is resolved using the method of omegaEqn solve().

```
165    fvScalarMatrix omegaEqn
166    (
167        fvm::ddt(omega)
168      + fvm::div(phi, omega)
169      - fvm::laplacian(alphaOmegaEff, omega)
170    );
171
172    omegaEqn.relax();
173
174    fvOptions.constrain(omegaEqn);
175
176    omegaEqn.solve();
```

At the end of the scripts the density is updated taking into account the temperature and humidity contributions using the equation (1.4).

```
185    rhok = 1.0 - beta*(T - TRef) - betaOmega * (omega - omegaRef);
```

2.2 Evaporation boundary condition

2.2.1 Vapour concentration

The value of vapour concentration at the interface (ω_Γ) described in eq (1.8) is computed using the boundary condition of ω. The boundary condition is implemented in OpenFoam using the mixedFvPatchScalarField which is a boundary condition obtained from a combination of a constant value (refValue) and a constant gradient (refGrad), weighted by the fraction (valueFraction).

When the function updateCoeffs() is called for the ω boundary conditions the necessary parameters and variables (M_v/M_a, H, T and P_{sat}) are initialized

```
157 void Foam::vaporConcentrationFvPatchScalarField::updateCoeffs()
158 {
159     if (updated())
160     {
161         return;
162     }
163
164     Info << "*** updating omega "<< patch().name() << endl;
165
166         fixesValue_ = true;
167
168         scalar Mfrac=Mv()/Ma();
169
170         scalarField _Height =  Height();
171
172         scalarField Tred = Temperature() - 273.15;
173
174         scalarField _ps = (611.85 * exp ( 17.502 * Tred / (240.9 + Tred) ));
```

For each cell is checked the value of the fields H, if it is grater than 0 the value of ω at the interface is computed following the eq. (1.8)

```
176         forAll(patch_.faceCells(),fi){
177             if(_Height[fi] > 0){
178                 (*this)[fi]=(
179                         Mfrac * _ps[fi]
180                         /
181                         ( Patm_ - ((1.0 -Mfrac) * _ps[fi]) )
182                 );
183                 if((*this)[fi]<0) (*this)[fi] = 0;
```

The variable refValue is set ugual to ω_Γ for all the face cells and valueFraction is set to 1 wich means that the boundary will behave as a fixed value boundary condition.

```
186                 this->refValue()[fi] = (*this)[fi];
187                 this->refGrad()[fi] = 0.0;
188                 this->valueFraction()[fi] = 1.0;
```

If H is not greater than 0 refGrad and valueFraction are set to 0 so the boundary condition will work as a von Neumann b.c.

```
189         }else{
190                 this->refValue()[fi] = 0.0;
191                 this->refGrad()[fi] = 0.0;
192                 this->valueFraction()[fi] = 0.0;
193                 fixesValue_ = false;
194
195             }
196         }
```

When refValue, refGrad and valueFraction are set for both the conditions on H, the boundary is updated using the OpenFoam class mixedFvPatchScalarField

```
198     mixedFvPatchScalarField::updateCoeffs();
199
200 }
```

When valueFraction is set to 1 the function set the value of the face cells at the value refValue, and when valueFraction is 0 the function set the gradient on the boundary at the value refValue.

2.2.2 Evaporation/condensation velocity

The velocity of evaporation $\mathbf{U}_\omega$ is defined as a vector field which is 0 in all the domain except in the boundaries where it may assume different values. When the boundaries are updated all the variables needed for the computation of $\mathbf{U}_\omega$ are initialized

```
246  void Foam::velocityEvaporationCondensationFvPatchVectorField::updateCoeffs()
247  {
248          Info << "*** updating Uomega " << patch().name() << endl;
249
250          scalarField _omega ( omega());
251          scalarField _Domega (Domega());
252          scalarField _omegaGrad (omegaGrad());
253          scalarField _H (H());
```

The value of $\mathbf{U}_\omega$ is computed using eq. (1.10)

```
255          scalarField evaporationVelocity = -( _Domega/(1.0-_omega))*_omegaGrad;
```

In each face cells in wich H is 0 or less, $\mathbf{U}_\omega$ is set to 0

```
257          forAll(patch_.faceCells(),c){
258                  if (_H[c] <= 0){
259                          evaporationVelocity[c] = 0;
260                  }
261          }
```

$\mathbf{U}_\omega$ is set to be a vector normal to the surface

```
263            const vectorField n(patch_.nf());
264      vectorField::operator=(evaporationVelocity * n);
```

The boundary is updated using the OpenFoam class fixedValueFvPatchVectorField wich set the value of $\mathbf{U}_\omega$ equal to the variables evaporationVelocity.

```
266          fixedValueFvPatchVectorField::updateCoeffs();
267  }
```

2.2.3 Evaporation/condensation heating flux

As shown in the explanation of TEqn.H, the source term is implemented using a scalar field EvCoHF which corresponds to the norm of $\mathbf{q}$. Before updating the EvCoHF, the U_ω and H variables are initialized. Only the component of U_ω normal to the boundary is used.

```
309          scalarField ha (H());
310
311          tmp<scalarField> UomegaNormal (Uomega() & patch().nf() );
```

20

newGradient is a scalar field defined as the product of L_ρ and U_ω.

```
311          scalarField newGradient (Lrho_ * UomegaNormal());
```

If H is not greater than 0 there can not be evaporation so newGradient is set to 0 (SMALL is a OpenFoam's constant defined as 1e-6).

```
314          forAll(newGradient,fi)
315              {
316                      if( ha[fi] < SMALL)
317                      {
318                              newGradient[fi] = 0;
319                      }
320              }
```

At the end, the boundary of EvCoHF is updated as a fixed value boundary condition, using the value of newGradient

```
314          fvPatchScalarField::operator=(newGradient);
315
316      fixedValueFvPatchScalarField::updateCoeffs();
```

2.2.4   Film thickness

The field H, which described the film thickness, is used to define in which boundary cells evaporation is possible. This field is null in all the domain except in the boundary with the water film, where evaporation takes place. Here H has the value of the height of the water film. The value of the boundarys of H is updated using the function updateCoeffs(). If the value of H is greater than 0 the evaporation and condensation may occur so the function read the value of U_ω and the value of dt and with that compute the value of dh using the formula

$$dH = \mathbf{U}_\omega \cdot \hat{\mathbf{n}} \frac{\rho_{air}}{\rho_{water}} dt. \tag{2.6}$$

```
100  void filmThicknessFvPatchScalarField::updateCoeffs()
101  {
102          Info << "*** updating H "<< patch().name()<<endl;
103
104      const fvPatch& p = patch();
105      const label & thispatch = p.index();
106      vectorField n = p.nf();
107      const fvPatchVectorField& U_interface = db().lookupObject<volVectorField>(UName_).boundaryField()[thispatch];
108      const fvMesh& mesh = internalField().mesh();
109      scalar ratio = 0.001; // rho_air/rho_water
110      scalarField dh (this->size());
111      forAll(*this,c){
112              if ((*this)[c] <= 0) dh[c]=0;
113              else dh[c] = (U_interface[c] & n[c])*ratio*mesh.time().deltaT().value();
114          }
```

Then it updates the value of H.

```
115      scalarField::operator += (dh);
116  }
```

Chapter 3

Validation of the simulation approach

3.1 Channel flow settings

For the validation of the model is used the data from a DNS of a turbulent channel flow with a $Re_\tau = 395$, reported by Moser et al.[16]. Re_τ is the friction Reynolds number, defined as

$$Re_\tau = \frac{u_\tau \delta}{\nu} \tag{3.1}$$

where u_τ is the friction velocity, defined in therm of wall shear stress τ

$$u_\tau = \sqrt{\frac{\tau}{\rho}}. \tag{3.2}$$

The DNS is done on a channel flow with dry air without evaporation, to compare that with the simulation done with humidityBuoyantBoussinesquePimpleFoam g is set to 0 so that there is no buoyancy effect.

In this way, it is possible to validate the dynamical part of the solver, for the validation of the evaporation model were used the wall function proposed by Desouter et al. [8].

The case is an infinite channel between two walls on the top and bottom, perpendicular to the y-direction, and a body force along the x-direction. The simulation is made in a domain of $2\pi \times 2 \times \pi$, divided in a grid of 50 cells along the x coordinate, 90 along the y and 70 along the z.

The coordinate of the ξth cell follows the equation:

$$\vec{x} = \vec{x}\left(\vec{s}\left(\xi\right)\right). \tag{3.3}$$

The $s(\xi)$ function change for each direction, along the x and z coordinates the distribution of points is linear:

$$s\left(\xi\right) = \frac{\xi}{I} \tag{3.4}$$

β	3.3e-3	[1/K]	β_ω	0.63	-
T_{ref}	297.5	[K]	ω_{ref}	0	-
Pr	114.038	-	Sc	76.950	-
Pr_t	0.7	-	Sc_t	0.7	-
ρ	1.165	[kg/m³]	c_p	$1.005\dot{1}0^3$	[J/(kg K)]
u_τ	1	[m/s]	ν	2.53165e-03	[m²/s]
g	0	[m/s²]			

Table 3.1: Parameters used in the simulation of the channel flow for the validation of the model

where I is the number of points along the direction.

In the y coordinate (which is the direction perpendicular to the walls) is used a double-sided hyperbolic stretch, and the $s(\xi)$ function becomes:

$$s\left(\xi\right) = 1/2\left(1 + \frac{tanh\left(\delta\left(\xi/I - 1/2\right)\right)}{tanh\left(\delta/2\right)}\right) \tag{3.5}$$

where δ is a parameter set to 5.

The choise of the grid parameters is so that the first point along the y coordinate is within $y^+ = 1$ and there are 9 points within $y^+ = 10$, where y^+ is defined as

$$y^+ = y\frac{u_\tau}{\nu} = y \cdot Re_\tau. \tag{3.6}$$

The distance from two adiacent points in the plus coordinates parallel to the wall (defined analogously to y^+) is $\Delta x^+ = 49.6372$, $\Delta z^+ = 17.7276$.

The parameters used for the simulation are shown in table 4.1.5. u_τ is set to 1 m/s introducing a body force of 1 m/s². This is possible because the wall shear stress is proportional to the pressure gradient,

$$-\frac{\partial p}{\partial x} = \frac{\tau_w}{H}. \tag{3.7}$$

In this case $H = 1\,m$, so for the definition of u_τ, (3.2), the value of the body force (F) is equal to the value of u_τ^2:

$$F = -\frac{1}{\rho}\frac{\partial p}{\partial x} = \frac{1}{\rho}\frac{u_\tau^2\rho}{H} \tag{3.8}$$

The initial conditions of velocity, pressure, turbulent viscosity and vapour concentration are set to 0. The temperature on the top wall is set to 285 K and the bottom wall is set to 310 K, while the points inside the domain start from 297.5 K.

The boundary conditions are set cyclic for the lateral boundaries. On the walls, the boundary conditions are set: no slip for the velocity; constant values for the temperature; for the field which described the evaporation are used the boundary condition

23
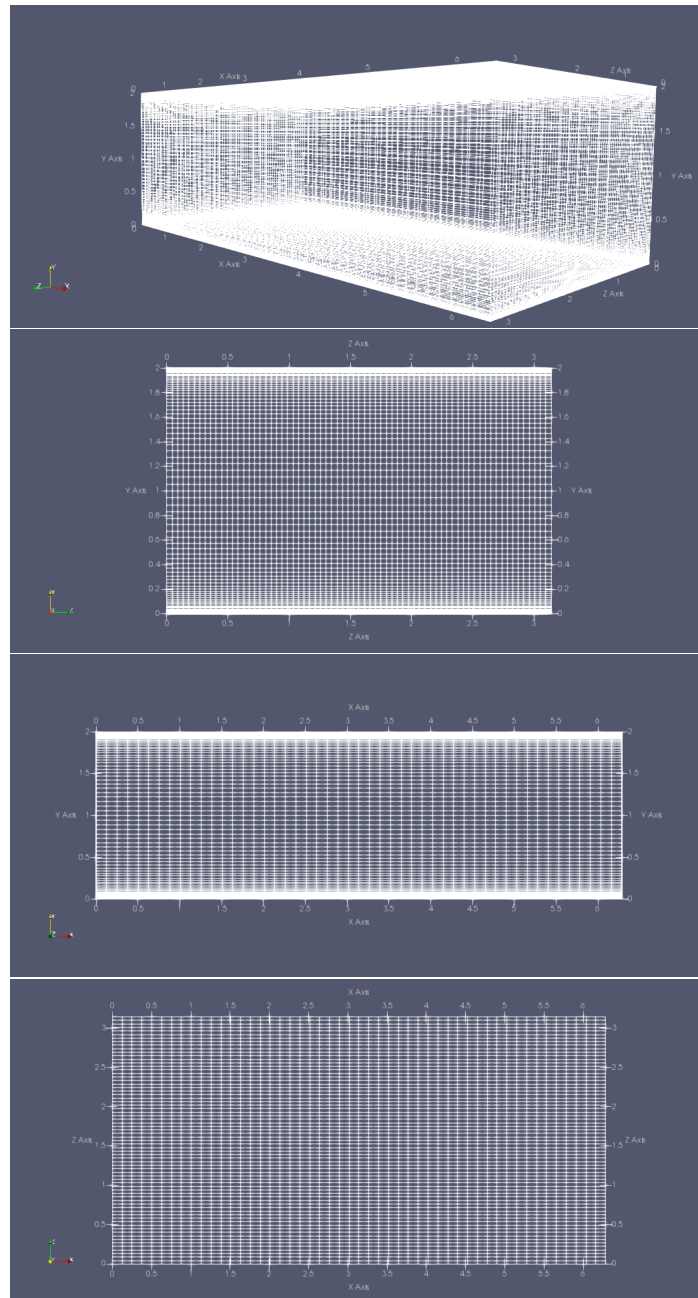
Figure 3.1: Copmputational domain, from top to bottom: the entire domain; the yz face; the xy face; the xz face.

Smagorinsky	
C_k	0.026
C_ϵ	1.0
C_s	0.065
WALE	
C_w	0.325

Table 3.2: Parameter used in the turbulence models

described in Chapter 2; and for the other fields are set to zero gradient.

The case was run with three different turbulence models Smagorinsky, WALE and dynamic Lagrangian, in Table 3.1, are reported the values of the parameters used in the turbulence models.

3.2 Validation of turbulence models

The channel flow is a well-known case study for the analysis of turbulent flows near a wall. As shown by Piomelli [21] near the wall the flux is divided into three different layers. For $y^+ < 5$ there is the viscous sublayer, where U^+ (which is the mean velocity divided by the friction velocity) have a linear profile. Above the viscous layer, up to about 30 y^+, is the buffer layer, where the peak of the kinetic energy is located. Over 30 y^+ there is the logarithmic layer where U^+ follow a logarithmic profile.

Figure 3.2 shows the profile of U^+ of the simulation with the three different turbulence models.

All the data produced by the simulations are averaged over all the domain in the x and z direction, and over 150 time steps of 0.1 s each.

For $y^+ < 5$, the profile is fitted with a linear function:

$$U^+(y^+) = a + by^+ \tag{3.9}$$

with $a = 0.019$ and $b = 0.97$.

For $60 < y^+ < 110$, the profile is fitted with a loarithmic function:

$$U^+(y^+) = c + d\,log(y^+) \tag{3.10}$$

with $c = 5.2$ and $d = 2.5$.

In the viscous layer, the profile of the DNS is well reproduced by the simulations. In the logarithmic layer, where the grid points are further away from each other, there is a greater difference between the simulations profile and the DNS. In the centre of the channel the velocity of the simulations is greater than the DNS, so the turbulent viscosity is underestimated. There could be several causes of the underestimation of
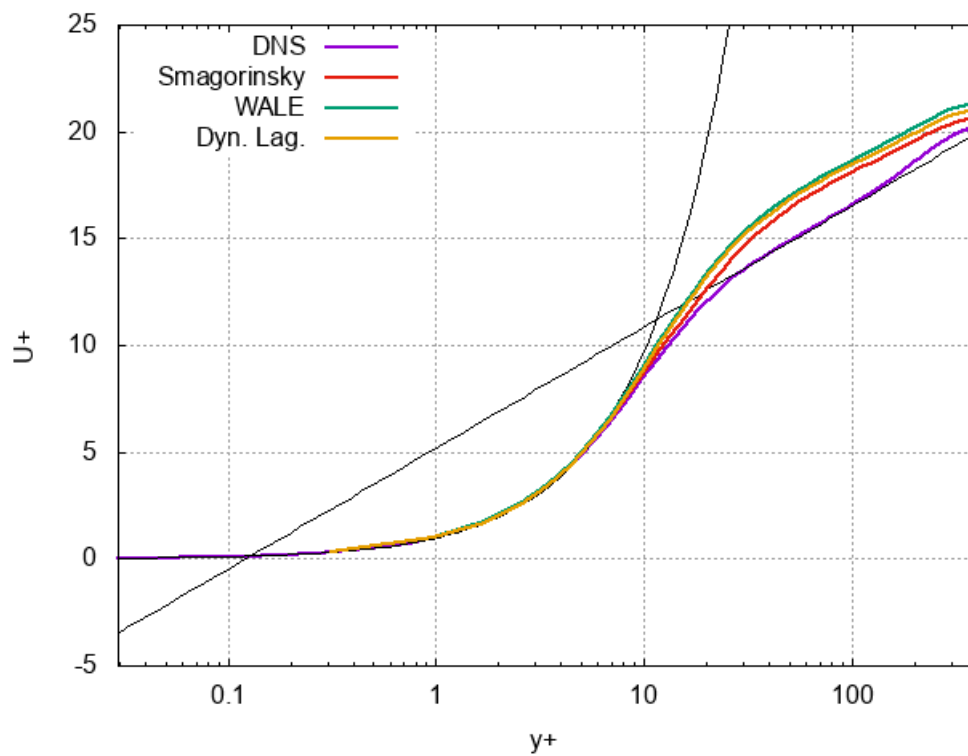
Figure 3.2: Profiles of U^+ in function of y^+ for the three turbulence models and the DNS, the x-axis is on a logarithmic scale, the fitted lines are plotted in black

turbulent viscosity, as turbulence plays a fundamental role in channel flow dynamics. Nevertheless, the qualitative behaviour of u is reproduced by the simulations, where the three different layers (viscous, buffer and logarithmic) can be clearly seen.

Figure 3.3 shows the profile along y of the Reynolds stresses diagonal component, $\langle u_i'^2 \rangle$, comparing the three different turbulence models to the DNS. In the streamwise direction, the Reynolds stresses are an order of magnitude greater than in the other direction, and the turbulence models produce greater Reynolds stresses than the DNS, this is probably due to the underestimation of the turbulent viscosity which produces faster motion with greater fluctuation. In the other directions, there is an underestimate of the Reynolds stresses. The turbulence model which better reproduce the profile is the Smagorinsky which is known to be a high dissipative model so it compensates for the underestimation of viscosity better.

3.3   Validation of the evaporation model

In order to test the evaporation model in the running case, the two walls of the channel flow have different temperatures (310K e 285K) and are covered with a film of water in which may occur evaporation and condensation. In the simulation is ignored the buoyancy contribution so $g = 0$. In Figure 3.4 are shown the profile of ω and T, obtained with the Smagorinsky turbulent model, which is the one that better reproduces the dynamic inside the channel. For a turbulent flow over a boundary with an evaporating liquid film, Desouter [8] proposed wall function of the type:

$$y^+ < y_T^+ : \zeta = a_\zeta + b_\zeta \, y^+ \tag{3.11}$$

$$y^+ > y_T^+ : \zeta = c_\zeta + d_\zeta \, log(y^+) \tag{3.12}$$

where ζ is the concentration of the evaporating fluid (in this case ω) and y_T^+ is a threshold value that divides the linear and logarithmic regions.

For $y^+ < 5$ the profile is fitted with a linear function, eq. 3.11, obtaining $a_\zeta = 0.39$ and $b_\zeta = -95 \cdot 10^4$.

For $60 < y^+ < 110$ the profile is fitted with a logarithmic function, eq. 3.12, obteining $c_\zeta = 0.031$ and $d_\zeta = -0.001$.

Figure 3.4 show the profile of ω with the two fitting line, in function of y^+, the vertical axis is inverted because it is the profile near the bottom wall where the water is evaporating from the hot wall, so ω decrease with height.

In the same article, Desouter [8] proposed also a wall function for the temperature (T) of the type:

$$y^+ < y_T^+ : T = a_T + b_T \, y^+ \tag{3.13}$$

$$y^+ > y_T^+ : T = c_T + d_T \, log(y^+). \tag{3.14}$$
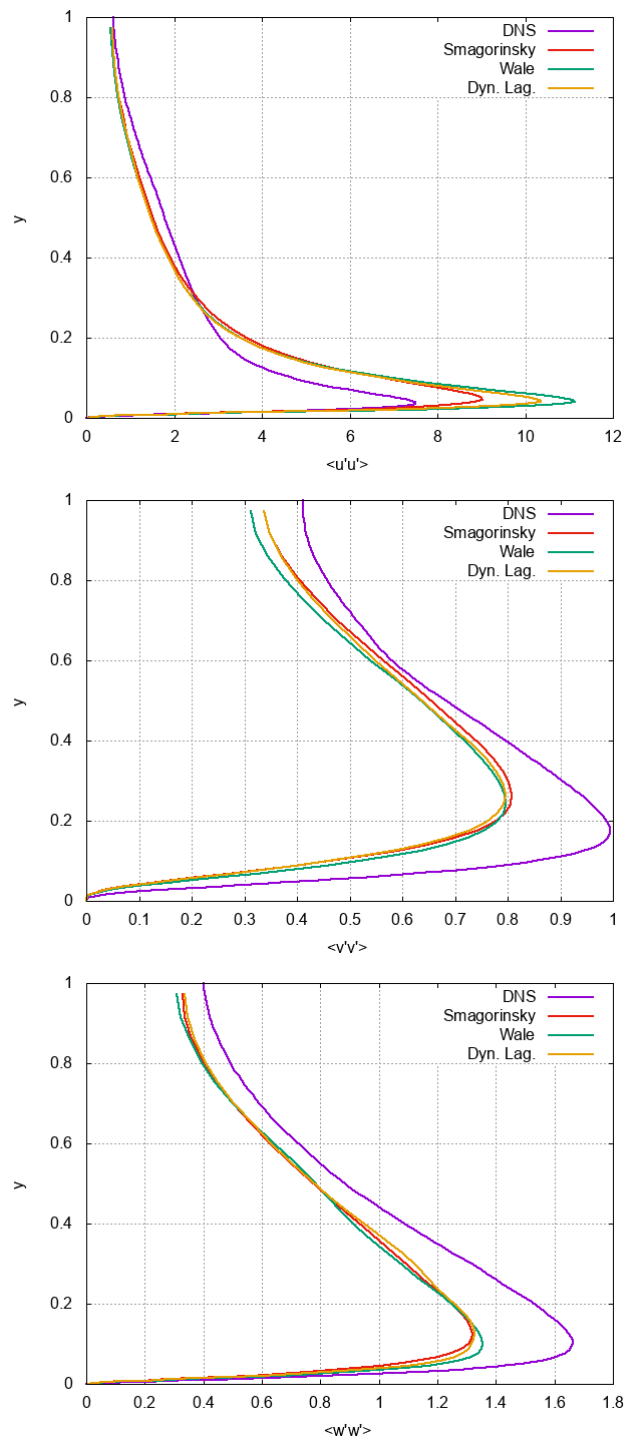
Figure 3.3: Profile along y of the diagonal term of the reynolds stress, for the DNS and the three turbulence models: top $\langle u'u'\rangle$; middle $\langle v'v'\rangle$; bottom $\langle w'w'\rangle$.

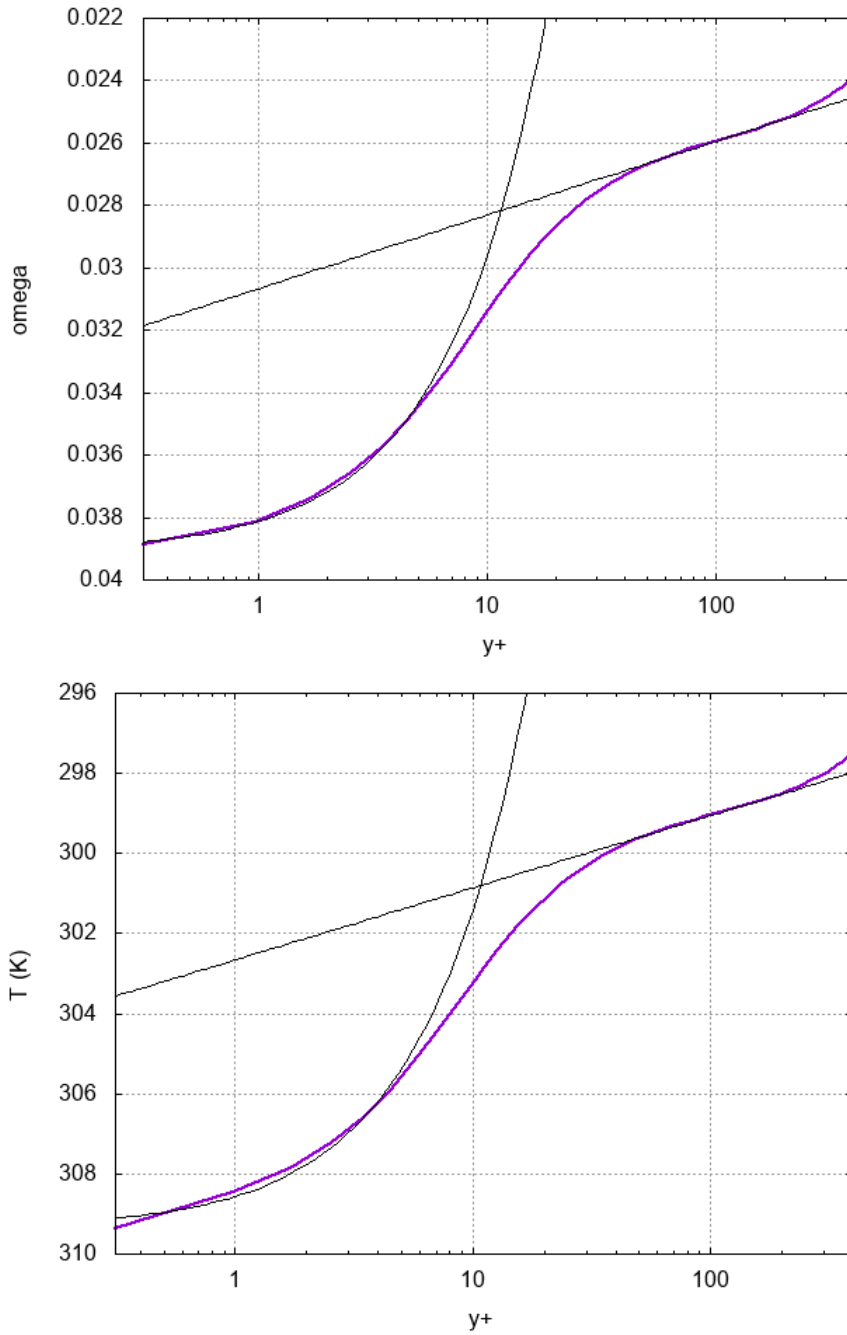Figure 3.4: Profile of T (top) and ω (bottom) in function of y^+, the x axis is in logarithmic scale, the fitted lines are plotted in black.

Figure 3.4 shows the profile of the temperature near the bottom wall (the vertical axis is inverted).

The temperature profile is fitted with a linear funcion, eq. 3.13, for $y^+ < 5$ obteining $a_T = 309$, $b_T = -0.80$. For $60 < y^+ < 110$, the temperature profile is fitted with a logarithmic function, eq 3.14, obtaining $c_T = 303$ and $d_T = -0.78$.

Both the temperature and vapour concentration follow a linear profile in the viscous sublayer, and a logarithmic profile in the logarithmic sublayer.

The model has been validated using the wall functions due to the lack of experimental data or DNS evaporation model. The model correctly reproduced the temperature and vapour behaviour near the wall, so it has correclty reproduced the evaporation from a water film in a turbulent flow.

Chapter 4

Street canyon simulations and results

4.1 Case study description

The case study is an infinite array of urban street canyons. Each canyon consists of two square buildings delimit a road of infinite lenght, at the center of the road there is an urban channel. Above the canyon, a wind current is imposed perpendicular to it. This simplified setting is intended to reproduce an urban area crossed by a waterbody. The presence of the evaporating waterbody can change the temperature and vapour concentration of the air. Both temperature and vapour concentration are treated as active scalars, which can therefore influence the dynamics of the system.

Two different configurations have been studied: one in which the water temperature is higher than that of the air, and another in which the water is colder than air. The first could represent a nocturnal situation in which the air undergoes rapid cooling due to the cessation of solar radiation while the thermal inertia of the water causes it to remain at a higher temperature. The second could represent a diurnal situation in which rapid heating due to solar radiation causes the air to have higher temperatures than water.

4.1.1 Geometry

Figure 4.1 outlines the geometry of the case. The road and the buildings wide is $W = 1m$ and the buildings high is $H = 1m$. The aspect ratio, which is the ratio between W and H, of the canyon is $a = 1$. The streamwise direction, perpendicular to the street, is x, the spanwise direction is y and the vertical direction is z. $z = 0$ is the plan of the street and $x = 0$ is a plan that cuts one of the two buildings in half along the streemwise direction. The system is symmetrical along the y direction. The computational domain is a parallelepiped starting from the origin ($x = 0, y = 0, z = 0$) long $2H$ in the streamwise direction, deep $2H$ in the spanwise direction and high $3H$ in the vertical direction. The
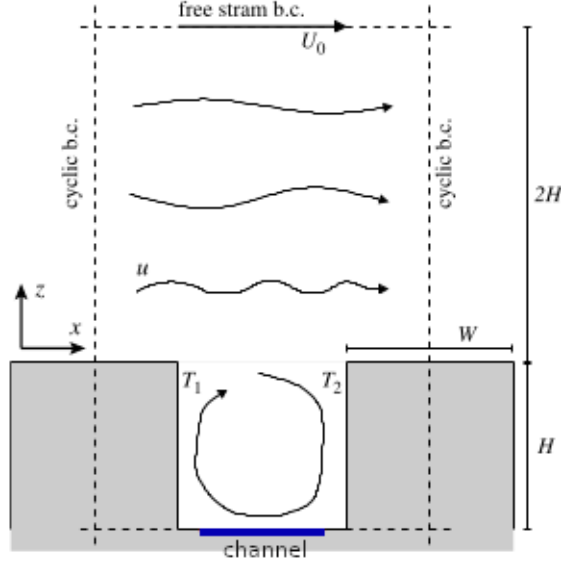
Figure 4.1:

street is located at $0.5 < x/H < 1.5$ and $z/H = 0$. The channel is $0.7m$ wide, located in the middle of the street at $0.65 < x/H < 1.35$ and $z/H = 0$. The boundary conditions on the front plane $y/H = 0$ and the back plane $y/H = 2$ are set cyclic to simulate a system of infinite depth in the spanwise direction. The boundary conditions on the inflow plan $x/H = 0$ and outflow plan $x/H = 2$ are set cyclic to simulate an infinite array of canyons. The top boundary is located at $z/H = 3$.

4.1.2 Computational grid

The computational domain is discretised using a grid with 1,592,562 cells. Figure 4.2 shows the computational mesh used. Near the solid surfaces the mesh is denser so that the first cell center is at $y^+ < 1$ (where y^+ is computed in the direction normal to the surface).

4.1.3 Boundary conditions

The boundary conditions of the velocity field are: no slip for the street, the channel, the buildings surfaces, and fixed at the value $U_0 = (0.2, 0, 0)m/s$ at the top boundary. The boundary conditions of the pressure field are set to zero gradient for the street, the channel, the buildings surfaces and the top boundary. The boundary conditions of the subgrid-scale eddy viscosity are set zero gradient for the street, the channel, the
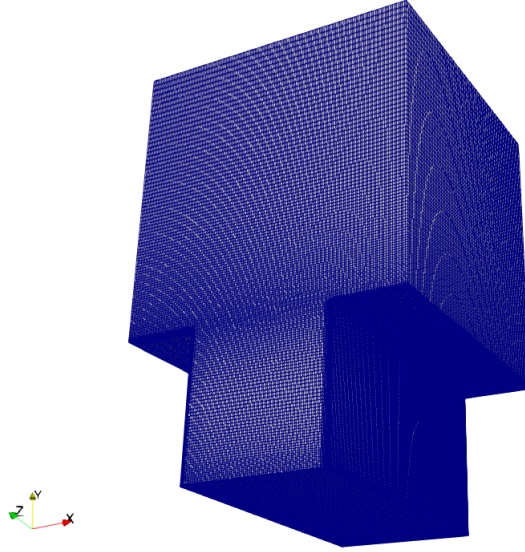
Figure 4.2: Overview of the computational mesh.

buildings surfaces and the top boundary. The boundary conditions of the temperature field are set fixed to the value $T_0 = 25°C$ for the street, the buildings surfaces and the top boundary. For the channel the temperature boundary condition is different for the two configuration: in the hot channel case the temperature is fixed at $T_{hot} = 27.5°C$ while in the cold channel case the temperature is fixed at $T_{cold} = 22.5°C$. In both configurations, there is an absolute difference of temperature $\Delta T = 2.5°$C. The boundary conditions of vapour concentration are set at zero gradient for the street and the buildings surfaces, while in the top boundary is fixed at the constant value $\omega_0 = 0$. For the channel boundary condition of the vapour concentration is used the boundary condition described in section 2.2.1. The field used for simulate the evaporation: film height, evaporation velocity and evaporation heating flux; are defined only on the channel boundary and the boundary conditions used are described in sections 2.2.2, 2.2.3, 2.2.4.

4.1.4 Initial conditions

Velocity and subgrid-scale eddy viscosity fields fully developed in the same geometry without the presence of the channel and evaporation, are used as initial conditions of that fields. The temperature field initial condition is T_0 in the entire domain. The vapour concentration field initial condition is ω_0 in the entire domain.

4.1.5 Physical parameters

The parameters used in the simulations are shown in Table 4.1.5. From the parameters

β_T	3.3×10^{-3}	[1/K]	β_ω	0.63	-
T_0	298.15	[K]	ω_0	0	-
Pr	2.220×10^{-5}	-	Sc	3.29×10^{-5}	-
Pr_t	0.7	-	Sc_t	0.7	-
ρ	1.165	[kg/m^3]	c_p	1.005×10^3	[J/(kg K)]
g	9.81	[m/s^2]	ν	1.568×10^{-5}	[m^2/s]

Table 4.1: Parameters used in the simulation of the street canyon

used is possible to define some non-dimensional numbers in order to describe the dynamical and thermal regimes of the simulations. The turbulent state of the air is described by the Reynolds number, which is computed using the air viscosity, the wind velocity at the top of the domain and the building height (H):

$$Re = \frac{U_0 H}{\nu}. \tag{4.1}$$

In that simulations, the $Re = 2.0 \times 10^4$ which is smaller than the normal atmospheric value (it is used smaller building and velocity), however, as Lup Wai et al. [4] have shown, the canyons with aspect ratio $a = 1$ are independent of Re for $Re > 12,000$.
The Reynolds number does not take into account the thermal effect and the natural convection produced by the buoyancy due to the temperature and moisture. To describe the thermal contribution in the natural convection is used the Grashof number:

$$Gr_T = \frac{g \beta_T \Delta T H^3}{\nu^2}. \tag{4.2}$$

That definition of Gr_T takes into account only the thermal contribution to the natural convection. In that simulations also ω contributes to the buoyancy. The ω difference ($\Delta\omega$) in the system is estimated using the difference between ω value at saturation at T_0, $\omega_s = 0.02$, and ω_0. Than the Grashof number for the vapour concentration contribution may be defined as:

$$Gr_\omega = \frac{g \beta_\omega \Delta\omega H^3}{\nu^2}. \tag{4.3}$$

From the Reynolds and the Grashof numbers is possible to compute the Richardson number, which describes the ratio of the buoyancy and inertial terms:

$$Ri = \frac{g \left(\beta_T \Delta T + \beta_\omega \omega_0 \right) H}{U_0^2} = \frac{Gr_T + Gr_\omega}{Re^2}. \tag{4.4}$$

Three different convection regimes are defined by the Richardson number: for $Ri \ll 1$ there is the forced convection regime, where the flow is driven by the inertial force, and natural convection is suppressed; for $Ri \gg 1$ there is the free convection regime, where dominates the buoyancy force; for $Ri \sim 1$ there is the mixed convection regime, where both buoyance and inertial therm are significant.

In that simulations $Gr_T = 8.2 \cdot 10^8$ and $Gr_\omega = 5.5 \cdot 10^8$, so the $Ri = 3.4$ so the contribution from inertial and buoyancy therm are both important to determine the evolution of the flow.

4.1.6 Numerical

The simulations are performed using the program humidityBuoyantBoussinesquePimpleFoam which is described in chapter 2. As turbulence model is used the Smagorinsky, which has produced better results in the validation reported in chapter 3. The maximum Courant noumber used is $Co_{max} = 0.5$. For the time derivative is used the OpenFOAM scheme backward which is a second order implicit scheme. For the spatial derivatives (gradients, divergences and laplacians) is used the OpenFOAM scheme Gauss linear, wich is a finite volume discretisation scheme which use a linear interpolation to compute the values at the faces centres from the cells centres.

4.2   First order statistic

In the following section are reported the results of the simulations for the two different configurations: the hot channel case, where the channel has a temperature of $27.5°C$; and the cold channel case where the channel has a temperature of $22.5°C$. The data of a simulation made by Cintolesi et al. [5], computed using the same geometry and parameters but in isothermal condition and withot the evaporating channel are also reported. This last case without the channel is used as referrence to investigate the impact of the channel.

All the data are averaged on all the cells in the spanwise direction along which the dynamic system is invariant. The time average is computed on 300 time steps of 1 s each.

The cases are described dividing it into four regions: the pedestrian region for $z/H < 0.2$; the internal region for $0.2 < z/H < 0.8$; the interface region for $0.8 < z/H < 1$; and the external region for $z/H > 1$.

4.2.1   Velocity field

For each case, the magnitude of the velocity field will be shown on a vertical section perpendicular to the spanwise direction, and the profiles of velocity components along

three vertical lines. Each velocity is divided by the velocity at the top of the domain U_0 and the each lenght is divided by the height of the buildings H, to make that non-dimensional. Figure 4.3 shows the streamlines of the velocity field and the magnitude of the velocity in the canyon, for the three cases: hot channel, cold channel and without channel. In the case without the channel, the dynamic inside the canyon is dominated by the main vortex with three smaller vortexes at the bottom-right, bottom-left and top-left, which rotate in the opposite direction to the main vortex. This configuration is typical of the urban canyons with an aspect ratio of 1 and the forcing of the upper wind [18]. In the two cases with the channel, the general dynamics is similar to the case without channel, with higher horizontal velocity in the pedestrian and interface regions for $0.8 < x/H < 1.2$, and higher vertical velocity in the interface region near the walls, $x/H < 0.7$ and $x/H > 1.3$. This show that the contribution of vapour concentration to the buoyancy (that will be shown is following sections) increase the intensity of the main vortex. In the cold channel case, the corner vortex at the top left does not develop.

Figure 4.4 displays the vertical profiles of the mean adimensional horizontal velocity for three different values of x, the first is halfway between the left wall and the channel at $x/H = 0.575$, the second is at the centre of the canyon at $x/H = 1$, the third is halfway the channel and the right wall at $x/H = 1.425$. The second profile is over the channel, while the others two are outside it. Overall, in the lower part of the canyon $z/H < 0.5$, all the cases exhibit horizontal motion in an opposite direction than the outside stream . In the higher part of the canyon, $0.5 < z/H < 1$, there are horizontal motion streamward, which become more intense in the external regions $z/H > 1$. In the hot channel case, are developed more intense velocities than the other cases, in particular in the pedestrian and the interface regions. In the left and right profiles over the floor at $x/H < 0.05$, the hot cannel case, shows areas of positive velocity related to the presence of secondary vortex. In the right profile at $0.7 < z/H < 1$, the hot channel case shows values that tend to zero, this is due to the right side of the top left vortex which is intersected from the line $x/H = 0.575$. In the cold channel case, in the pedestrian and interface regions, the velocties are more intense than the case without the channel but lesser than the hot channel case. In the right profile under $x/H = 0.1$ there are positive values due to the bottom right vortex. Outside the canyon, the velocity of the hot cannel and the cold channel cases are similar and are both greater than the case without the channel, so the vapour concentration increases the horizontal velocity also in the region outside the canyon.

Figure 4.5 shows the plofiles of the vertical velocity, for the same lines of the previous figure. All the cases exhibit the same qualitative behaviour, with high velocity in the internal region near the wall, and almost zero velocity in the middle of the canyon ($x = 1$) and outside the canyon. This is due to the main vortex, which has an upstream along the left wall, and a downstream along the right wall. The hot and cold channel cases have greater velocity near the lateral walls than the case without the channel due to the buoyancy produced by ω which will be shown in following sections. So higher value of
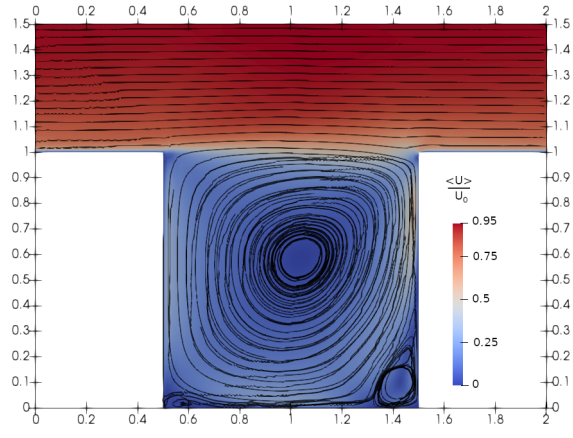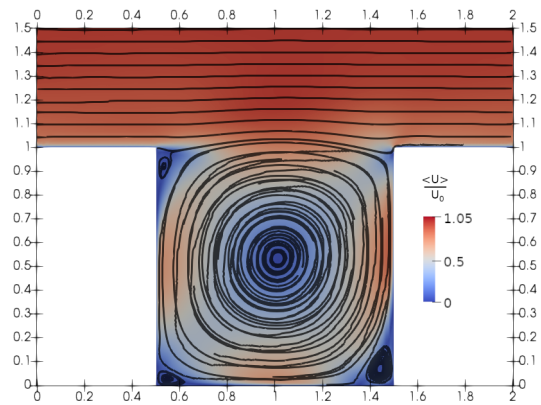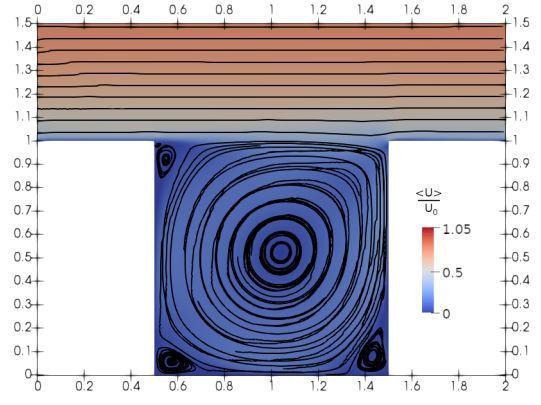
Figure 4.3: Stream lines (black lines), and magnitude values (background color) of the velocity fields, from top to bottom: the case withot the channel; the hot channel case; the cold channel case.
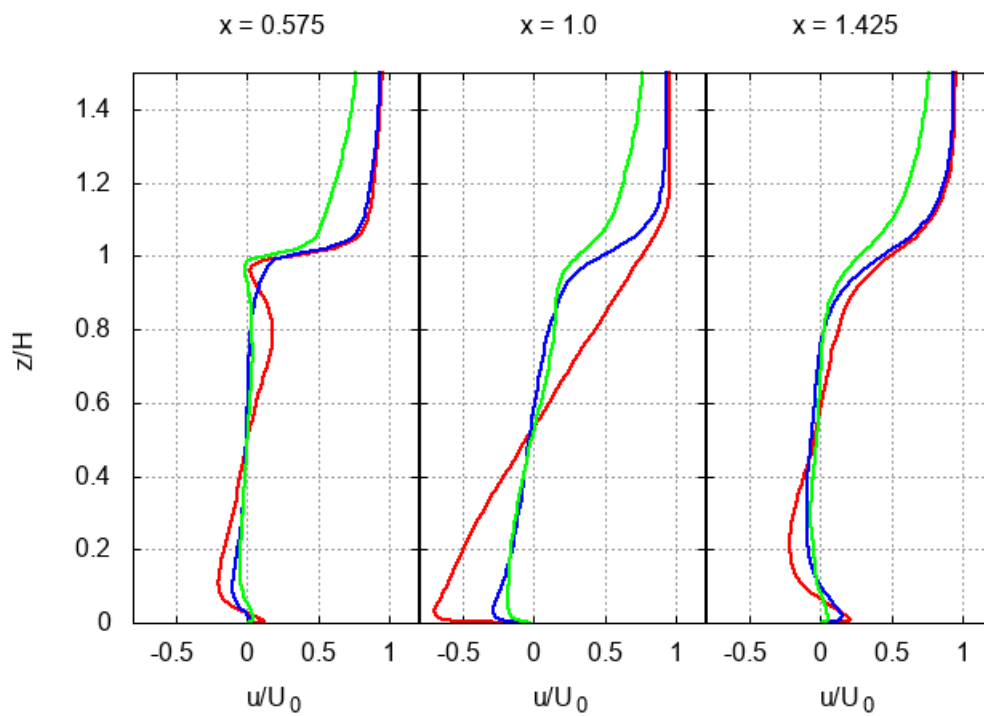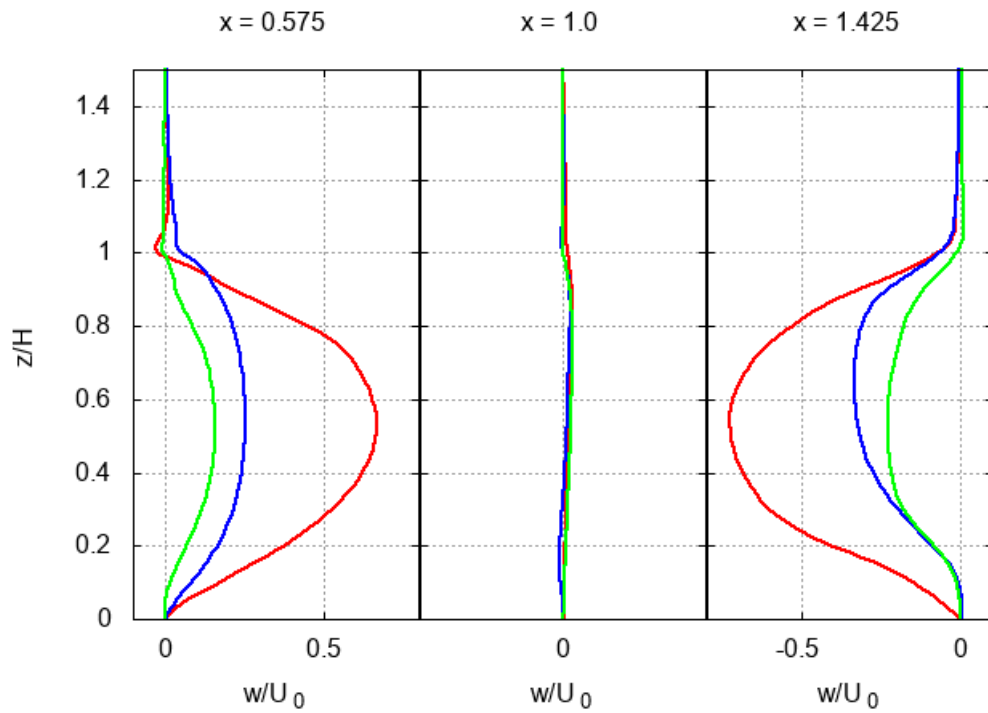
Figure 4.4: Vertical profiles of orizzontal mean adimensional velocity for the three cases: hot channel (red lines), cold channel (blue lines), without channel (green lines); for three different position: near the left wall (left plot), centre of the canyon (middle plot), near the right wall (right plot).

Figure 4.5: Vertical profiles of vertical mean adimensional velocity for the three cases: hot channel (red lines), cold channel (blue lines), without channel (green lines); for three different position: near the left wall (left plot), centre of the canyon (middle plot), near the right wall (right plot).

vapour concentration increase the upstream curent and then the circulation of the main vortex producing higher velocity inside the canyon.

4.2.2 Temperature field

The temperature field is made non-dimensional subtracting the initial environment temperature, T_0, and dividing for the absolute value of the difference between the channel temperature and T_0.

$$T^* = \frac{\langle T - T_0 \rangle}{\Delta T} \tag{4.5}$$

Figure 4.6 shows the values of the temperature inside the canyons for the hot and cold channel cases. In both cases there is a strong gradient immediately over the channel, due to the cooling effect of the evaporation, then the cold air is transported along the left wall by the upstream and diffused over the whole domain, where have uniform values. There is no positive value, so in both cases the presence of the channel produce a cooling effect on the environmental temperature. In all the domain, the cold channel case shows lower values than the hot channel case.

Figure 4.7 displays the profiles of T for the two cases with the channel at the same values of x/H used in the previous section. In the central profile, over the channel $z/H \simeq 0$, both cases show temperature colder than the initial temperature T_0. This means that also in the case with the hot channel the temperature sink in equation (1.5) due to the evaporation, dominates over the diffusive term. This produces a discontinuity with the boundary, where the temperature is set constant at the channel temperature, and the first computational cell, where the sink therm produces colder themperatures. That discontinuity is not physical and it is due to the model hypothesis used. In the rest of the domain, the impact of this effect should be reduced by the coupling of temperature and momentum equations. In the hot channel case the cooling effect of the evaporation in opposed to the heating effect of the channel temperature. This produce difference between 2-3% of ΔT from the starting temperature T_0. In the central profile, the cold channel case shows values $T^* < -1$ near the water surface. This is due to the evaporation which cooled the air below the channel temperature $T^*_{cold} = -1$. In the left profile the cold channel case shows lower temperatures than the right profile, this is due to the main vortex which transport cold air from over the channel to the updraft near the left wall. Inside the canyon, the cold channel case shows a difference between 10-20% of ΔT from the starting temperature T_0. Outside the canyon, the cold channel case shows a uniform difference of 7.5% of ΔT from the starting temperature T_0, so the presence of the cannel impact also the temperature outside the canyon.
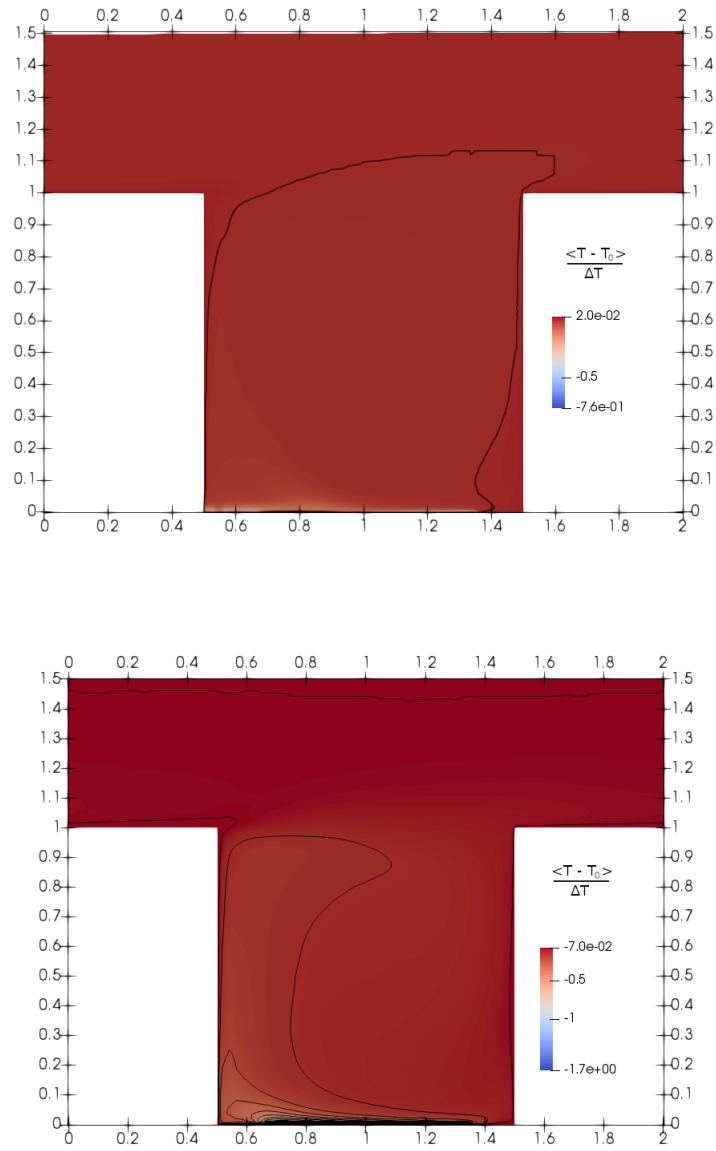
Figure 4.6: Values of the temperature fields of the hot channel case (top), and the cold channel case (bottom).
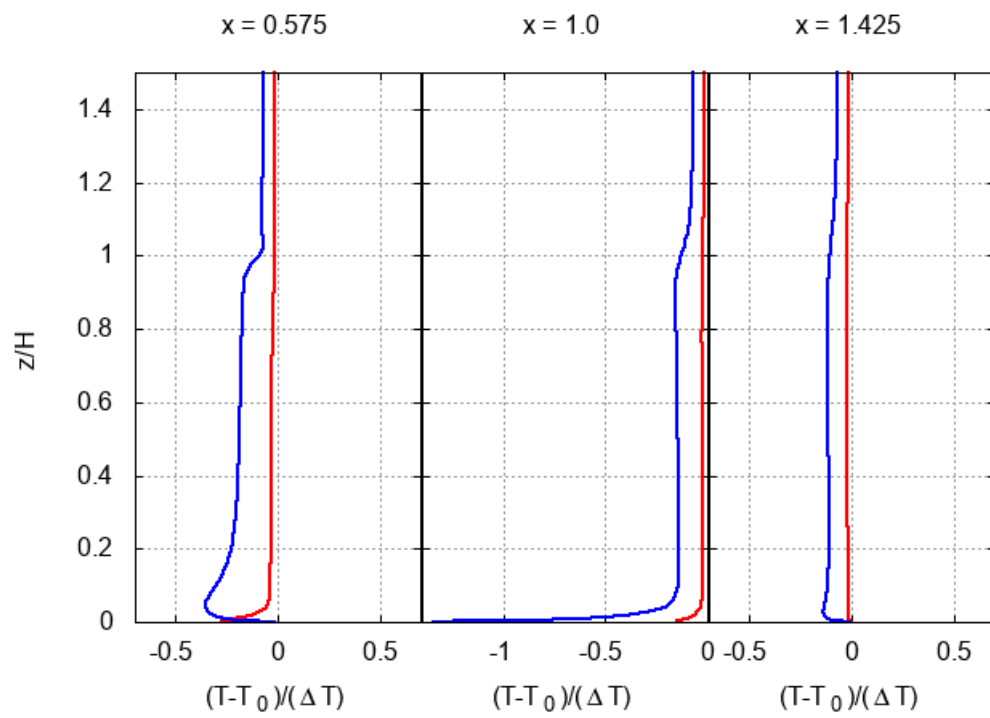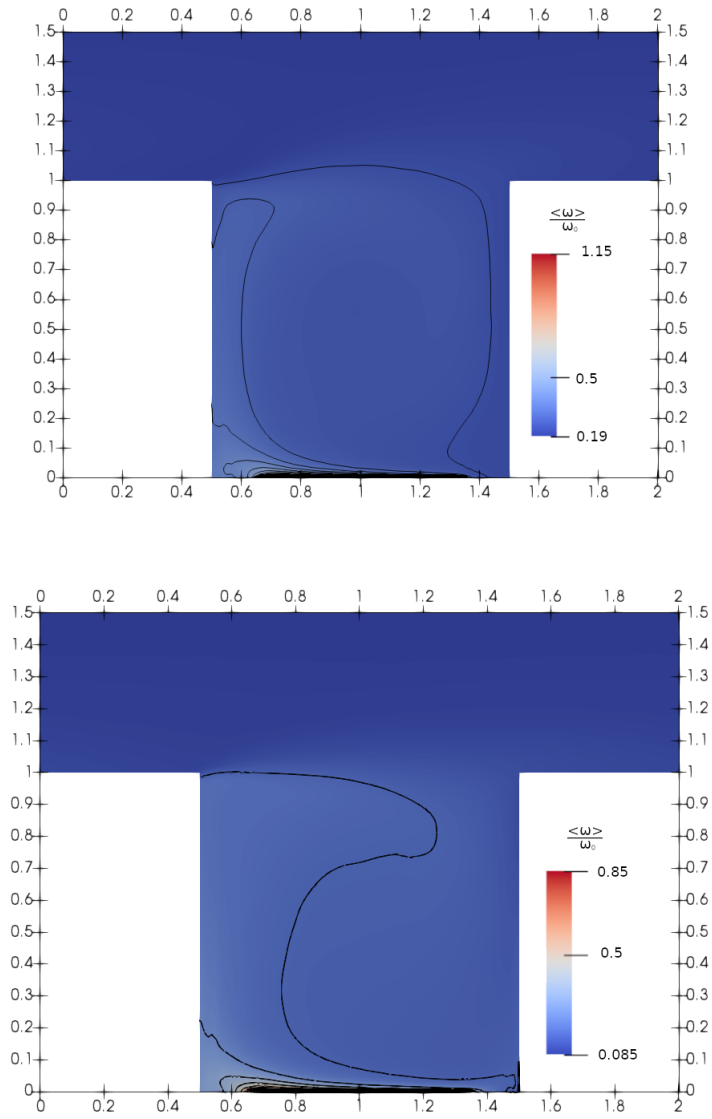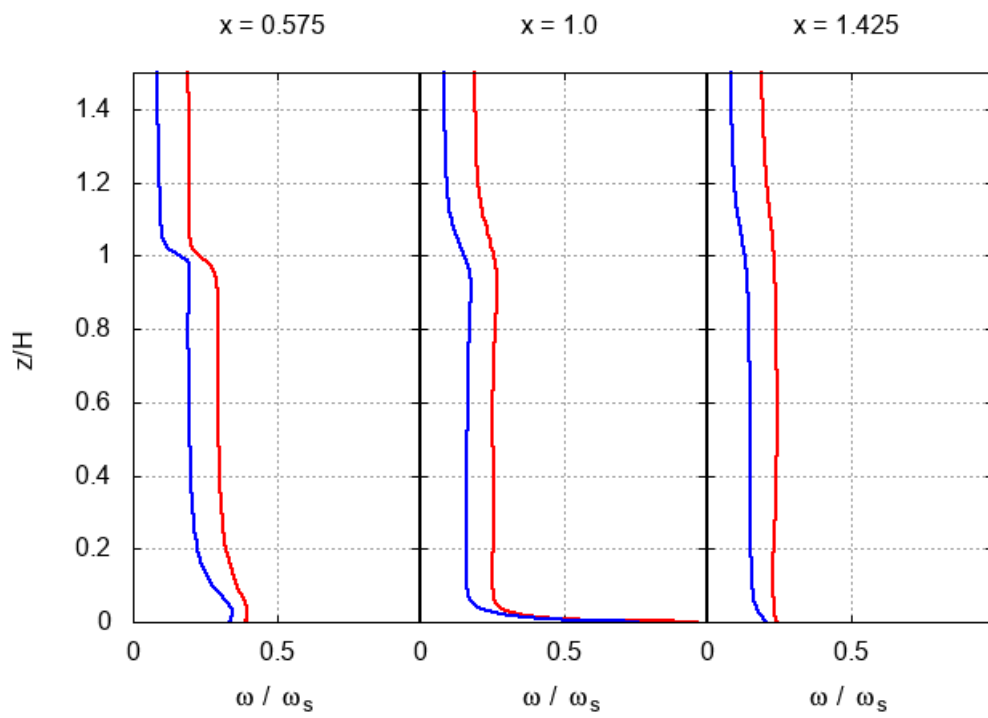
Figure 4.7: Vertical profiles of adimensional temperature for the two cases: hot channel (red lines), cold channel (blue lines); for three different position: near the left wall (left plot), centre of the canyon (middle plot), near the right wall (right plot).

4.2.3 Vapour concentration

The values of the vapour concentration field are divided to the vapour concentration at saturation ω_s at the temperature T_0, to made it non-dimensional.

$$\omega^* = \frac{\langle \omega \rangle}{\omega_s} \tag{4.6}$$

Figure 4.8 shows the vapour concentration distribution in the domain for the two cases with the channel. Overall, all the cases exhibit the highest values near the water surface, where the air is at saturation. On the rest of the domain the fields shows a rapid decrease, with higher values along the upstream near the left wall. The spatial distribution of the vapour concentration is qualitatively similar to the distribution of temperature, except in contact with the street and buildings surfaces, where the different boundary conditions show different behaviour.

Figure 4.9 shows the profiles of ω for three different values of x/H used also in the previous sections. In the central profile, immediately over the channel, both the cases shows values $\omega^* \simeq 1$ because in contact with the water the air is at saturation, then the profiles rapidly decrease due to the advection and turbulent diffusion. In the internal region and in the interface region, the values of ω^*, are uniform along the vertical, and higher in the left profiles than the right ones. Outside the canyon, both the cases shows uniform values smaller than that inside the canyon. In the left profile, where the values of ω^* inside the canyon are greater, the difference with values of the external region is greater than the other profile than the other two profiles. In all the profiles, the hot channel case show greater values of vapour concentration than the cold channel case. The warmer temperature of the channel produces more evaporation, than the vapour concentration is diffused from the motion producing higher values on the entire domain.
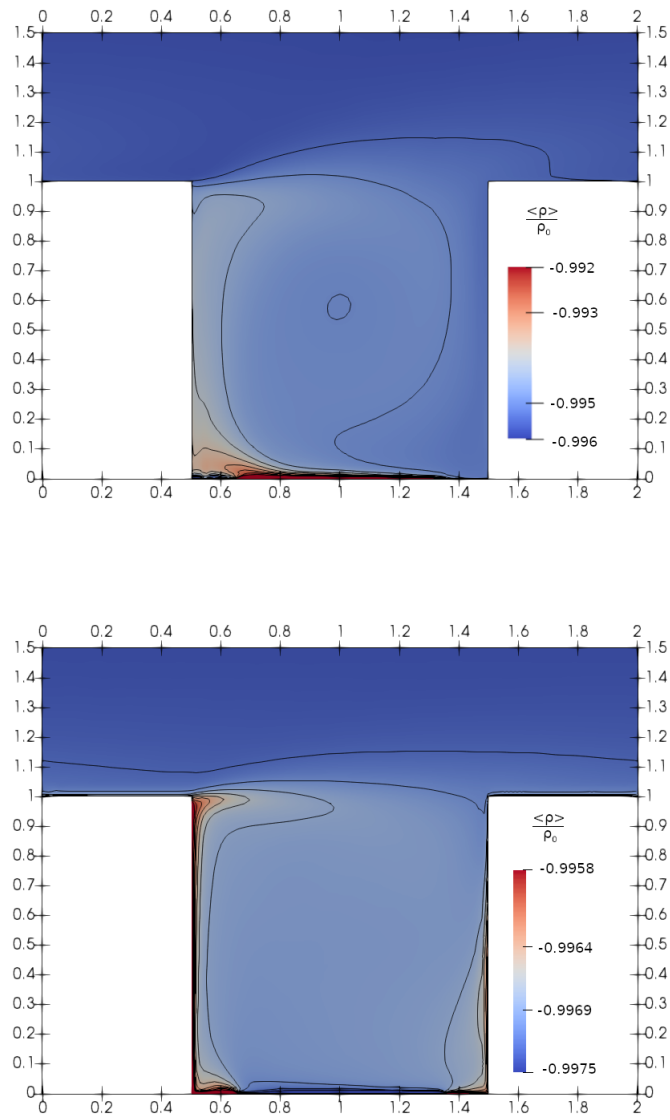
Figure 4.8: Values of the vapour concentration fields of the hot channel case (top), and the cold channel case (bottom).

Figure 4.9: Vertical profiles of vapour concentration for the two cases: hot channel (red lines), cold channel (blue lines); for three different position: near the left wall (left plot), centre of the canyon (middle plot), near the right wall (right plot).

4.2.4 Buoyancy force

The buoyancy force $(\rho/\rho_0)\mathbf{g}$ is divided by g to made it non-dimensional. As show in equations (1.2) and (1.4), the buoyancy force depends on both temperature and vapour concentration. Only the vertical component of the buoyancy force is not zero, so only that component will be discussed in this section. Figure 4.10 displays the values of the buoyancy force in the two cases with the channel. As shown in section 4.2.2, the difference between the hot channel case temperatures and the initial temperature T_0 are of the order of 2-3% ΔT. Section 4.2.3 show that the hot channel case have high values of vapour concentration. The high vapour concentration and low temperature values means that the buoyancy force, in the hot channel case, is possibly dominated by the ω contribution. The cold channel case show lower values of the buoyancy force, than the hot channel case. That case show high buoyancy values in contact with the left wall. This efect is probably due to the different idealized boundary conditions used for the temperature and vapour concentration fields. Indeed the temperature on the left building surface is set constant to T_0, while vapour concentration field has a zero gradient boundary condition. These high buoyancy values concentrated in a small region in contact with the wall $0.50 < x < 0.52/H$, could be the cause of the absence of the top left corner vortex in the cold channel case in Figure 4.3.

Figure 4.11 shows the vertical profiles of the buoyancy for the two cases with the channel at the values of x/H used in the previous sections. All the profiles shows uniform values in the internal and external region, in according with the profile of T and ω reported in Fiugure 4.7 and 4.9. The hot channel case show higher values in the left profile than the right profile. So in the left side, the buoyancy reduce the gravitational acceleration increasing the intensity of the updraft and the whole main vortex, as shown in section 4.2.1. The cold channel case, in the internal region, does not shows difference from left and right profiles. As shown previously in Figure 4.10, in that case the high values of buoyancy wich may contribute to the main vortex dynamics, are confined in a small region. That region does not intersect the line along which the profile are computed $x/H = 0.575$, except at $z/H = 1$ where the high buoyancy regions is deviated rightward by the external stream. At this hight the left profile shows a peak of buoyancy.

Figure 4.10: Values of the buoyancy force fields of the hot channel case (top), and the cold channel case (bottom).
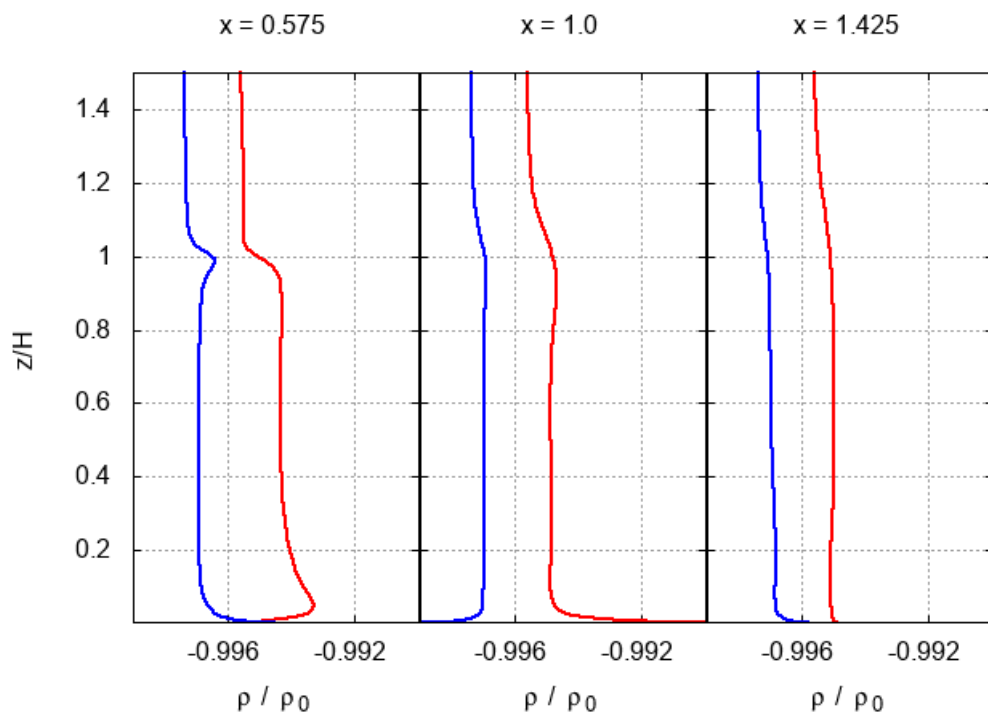
Figure 4.11: Vertical profiles of buoyancy force for the two cases: hot channel (red lines), cold channel (blue lines); for three different position: near the left wall (left plot), centre of the canyon (middle plot), near the right wall (right plot).

48

4.3　Second order statistic

4.3.1　Streamwise velocity variance

The streamwise velocity variance fields will be discussed in this section. For all the cases, the averaged field will be shown on a vertical section perpendicular to y, and the profiles of variances along three vertical lines. Each value is made non-dimensional dividing by U_0^2.

Figure 4.12 displays the values of the variaces of streamwise components of the normalized velocity. In all the cases there are high values of variance immediately over the interface region, $1 < z/H < 1.1$. In the hot channel case, there are also high values in the pedestrian level at the left side of the channel, $0.6 < x/H < 0.8$. In the cold channel case, the peak over the interface region is shifted towards the right side of the canyon, $x/H > 1$.

Figure 4.13 shows the profile of $< u'u' > /U_0^2$ for three different values of x/H for the three cases with hot and cold channel and without channel. All the profiles show their maximums over the interface region at $1 < z/H < 1.1$. In the hot channel case, the profile near the left wall shows a secondary peak in the pedestrian region, this peak is evident also in the other profiles of the same case, but with lower intensity. In the cold channel case, the variances are lesser intense than the hot channel case except the peak over the interface in the middle and right profiles, that shows higher values then the hot channel case. In both cases with the channel, the variances are greater than the case without the channel, so the increase of vapour concentration and buoyancy produce more fluctuations in the streamwise velocity.
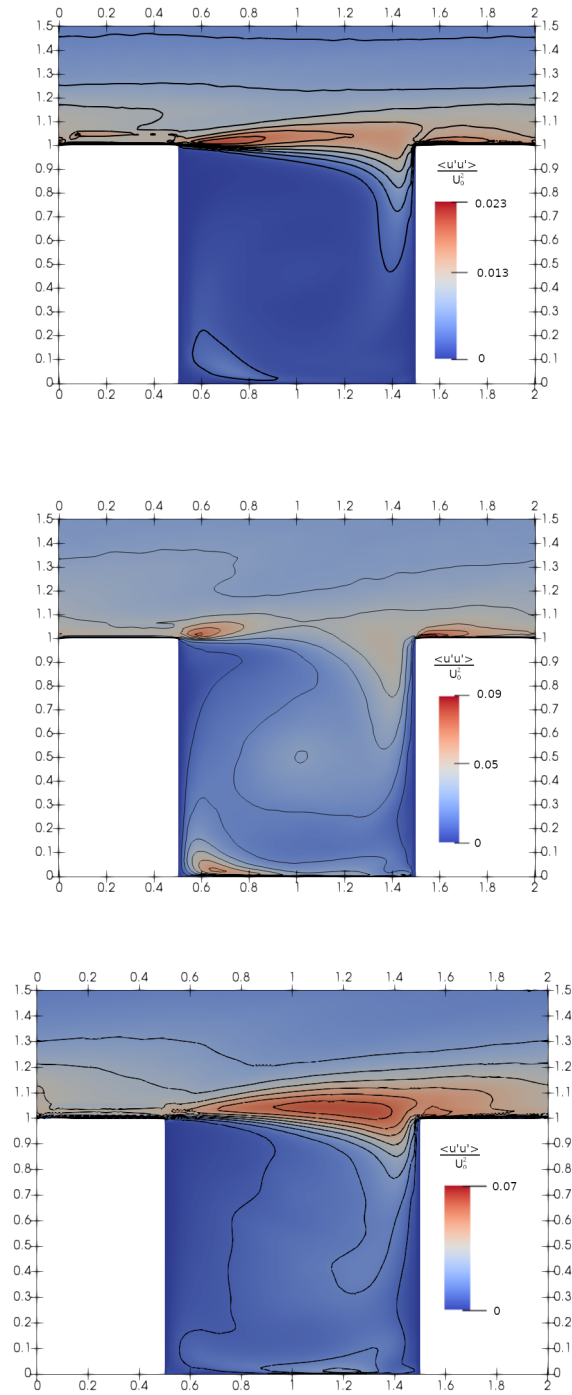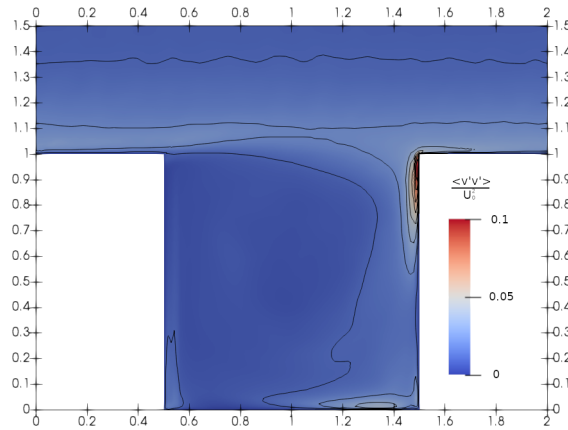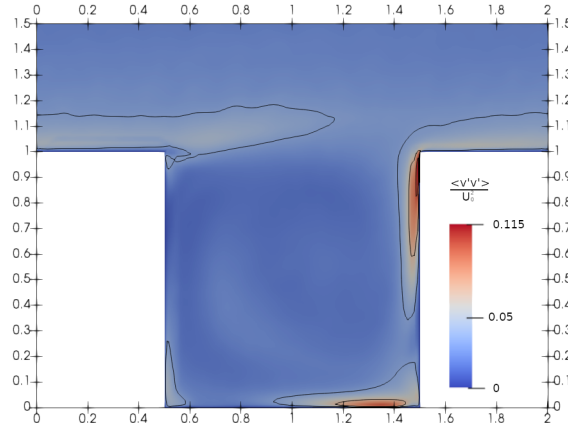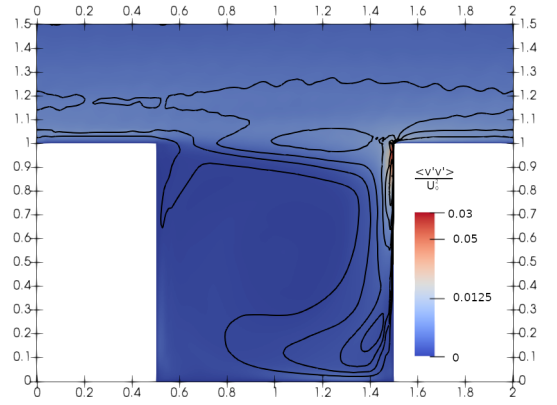
Figure 4.12: Values of the fields of variances of streamwise velocities, from top to bottom: the case withot the channel; the hot channel case; the cold channel case.
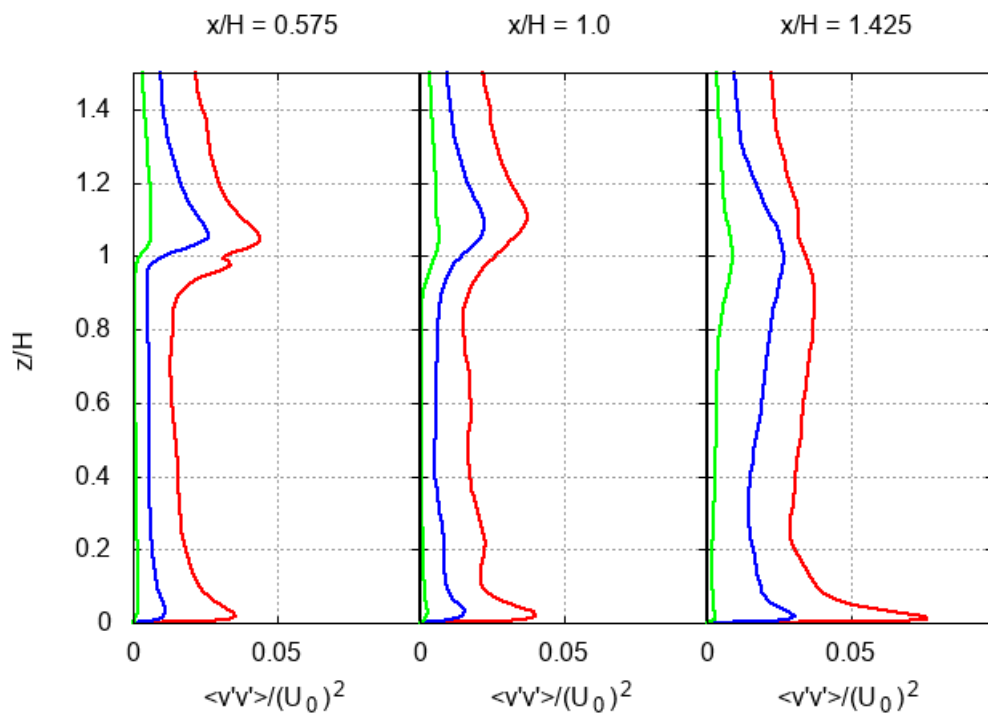
50
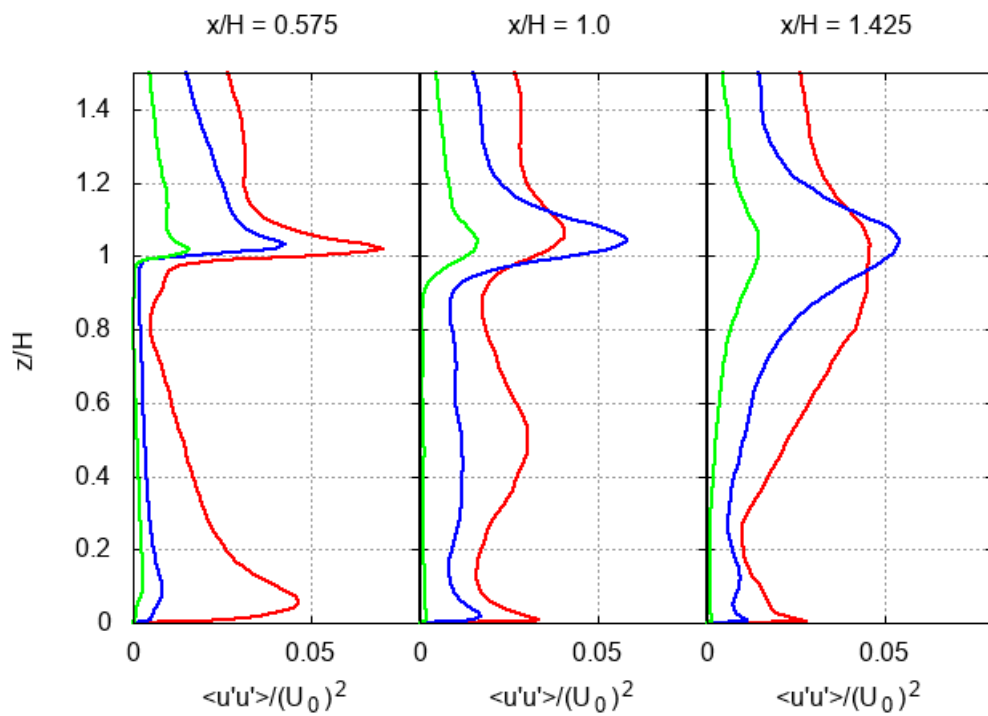
Figure 4.13: Vertical profiles of streamwise velocity variance for the three cases: without the channel (green lines), hot channel (red lines), cold channel (blue lines); for three different position: near the left wall (left plot), centre of the canyon (middle plot), near the right wall (right plot).

4.3.2   Spanwise velocity variance

The spanwise velocity variance fields has divided by U_0^2 to made it non-dimensional. Figure 4.14 shows the values of the spanwise normalized velocity variance, for the three cases.
In all the cases there is a maximum variance in the interface region near the right wall. In the cases with the channel, there is a secondary peak of variance, more evident in the hot channel case, immediately over the right side of the channel at $1.2 < x/H < 1.4$.

Figure 4.15 displays the profiles of the normalized spanwise velocity variance, for three different values of x/H. The profiles show two main peaks, one over the interface region, which is greater in the left profile, and one in the pedestrian region which have higher values in the right profile. The vertical line along the profile are plotted does not intersect the peak in the interface region near the right wall, which cannot be seen in the graphs.
The hot channel case shows higher values of the variance than the cold channel case, wich have greater values than the case without channel, this suggest the contribution of vapour concentration and so of buoyancy force in the increase of velocity variance.

Figure 4.14: Values of the fields of variances of spnawise velocities, from top to bottom: the case withot the channel; the hot channel case; the cold channel case.

Figure 4.15: Vertical profiles of spanwise velocity variance for the three cases: without the channel (green lines), hot channel (red lines), cold channel (blue lines); for three different position: near the left wall (left plot), centre of the canyon (middle plot), near the right wall (right plot).

4.3.3 Vertical velocity variance

The vertical velocity variance fields has divided by U_0^2 to made it non-dimensional. Figure 4.16 displays the value of normalized vertical velocity variance. In all the cases there are high values on the left side of the canyon at $x/H < 1.3$.

In the case without the channel, the peak on the right side is located between the interface and internal regions at $0.7 < z/H < 0.9$, where the horizontal motion are deflected inside the canyon.

In the hot channel case, the peak near the right wall is shifted down between internal and pedestrian regions at $0.05 < z/H < 0.45$. There are also high values of variance on the left side of the interface region. That difference may be due to the higher vertical velocity which produces more variances where the updraft and downdraft change the direction of motion.

In the cold channel case, the right peak of variances is located in the internal and pedestrian region near the right wall at $0.1 < z/H < 0.8$, which is at a greater height than the hot channel case, where the vertical motions are stronger, and a lower height than the case without channel where the vertical motions are weaker.

Figure 4.17 shows the vertical profiles of the variances of the vertical velocity for three different points along the x axis.

In the hot channel case, there is the main peak near the right wall in the pedestrian region, and a secondary peak near the left wall in the interface region.

In the cold channel case, there is only one peak at the bottom of the internal region $(z/H < 0.3)$ of less intensity than the hot channel case.

In both the cases with the channel, the values are greater than the case without the channel, also in the region outside the channel, showing the contribution of buoyancy in the production of variances of vertical velocity.
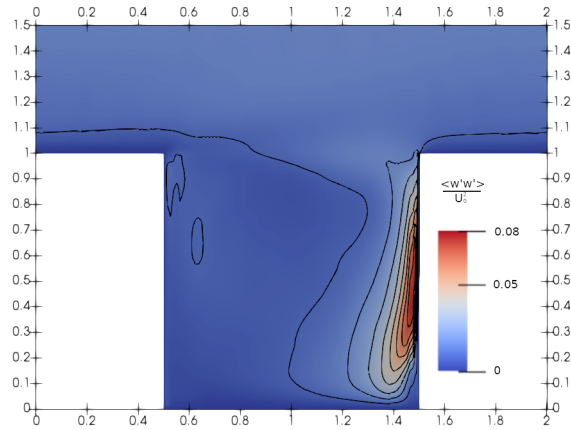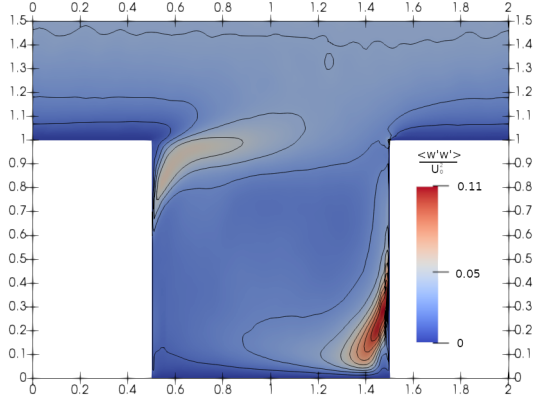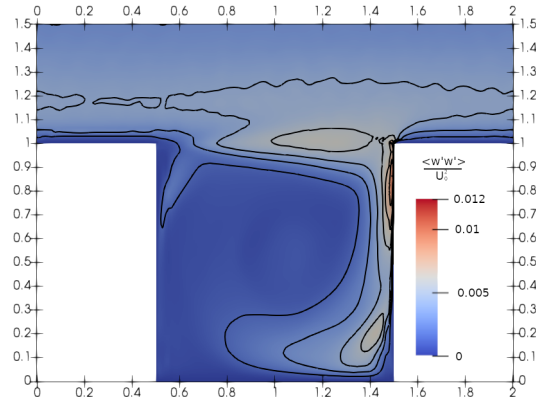
Figure 4.16: Values of the fields of variances of vertical velocities, from top to bottom: the case withot the channel; the hot channel case; the cold channel case.
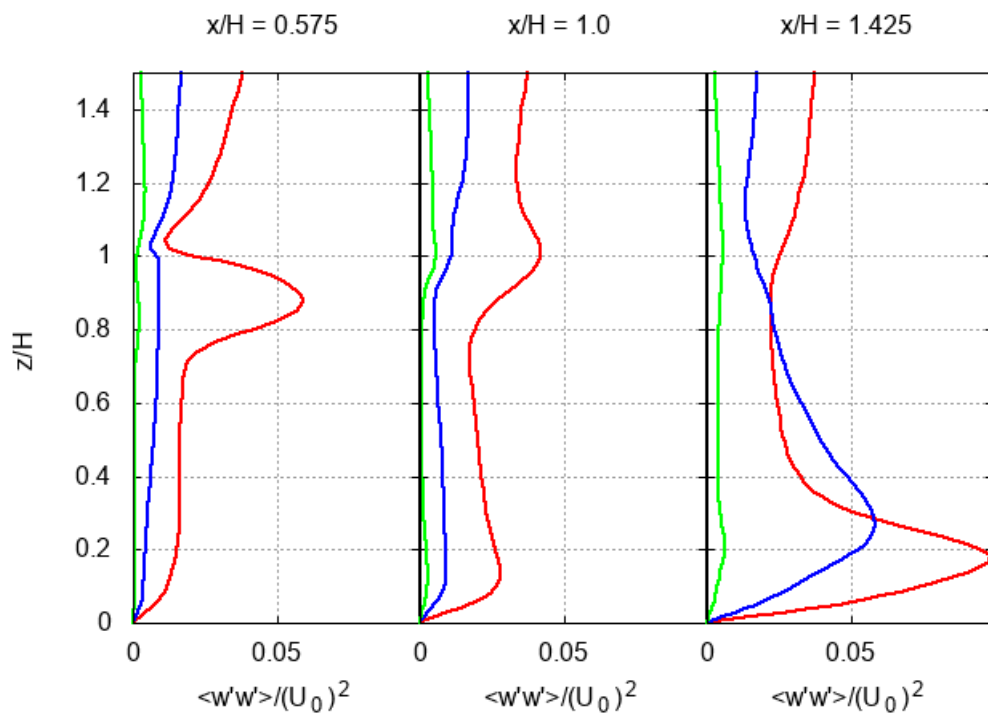
Figure 4.17: Vertical profiles of vertical velocity variance for the three cases: without the channel (green lines), hot channel (red lines), cold channel (blue lines); for three different position: near the left wall (left plot), centre of the canyon (middle plot), near the right wall (right plot).

4.3.4 Turbulent kinetic energy

In this section, the turbulent kinetic energy field will be discussed. The turbulent kinetic energy is defined as the sum of the variances of the three velocity component divided by 2, in this analisis the TKE will be divided it by U_0^2 to make it non-dimensional:

$$TKE = \frac{1}{2}\frac{\langle u'u' \rangle + \langle v'v' \rangle + \langle w'w' \rangle}{U_0^2}. \tag{4.7}$$

Figure 4.18 shows the vertical sections of the mean TKE spatial distribution, for the three cases: without the channel, with the hot channel and with the cold channel. All the cases show high values over the canyon at $1 < z/H < 1.1$. In the case without the channel, there are high-values in the top right corner of the canyon, until a height of $z/H > 0.8$. In the cold channel case values are higher than the previous, and the high value region near the right wall extends along the entire internal region, $z/H > 0.2$. In the hot channel case, the values are higher than the other cases, and the regions of high values extend on all the left side and continue leftward in the pedestrian region following the main vortex. The presence of the channel produces so higher turbulent motion, more intense in the hot channel case where buoyancy is stronger.

Figure 4.19 displays the profiles of the normalized turbulent kinetic energy, for three different values of x/H. The profiles in the different parts of the domain show similar behaviour, with high value in the pedestrian region and immediately over the interface. In the pedestrian region, the hot and cold channel cases show a peak that is greater near the right wall. Over the interface at $1 < z/H < 1.1$, all the cases have peaks in all the profiles, showing that in this region, the interaction between the main vortex and the external current produce turbulent motions. In all three profiles, the hot channel case have greater turbulent kinetic energy than the cold channel case which is greater than the case without channel. This show a strong contribution of buoyancy produced by vapour concentration in the production of turbulent motion in all the domain, also in the regions where the increasing of the medium velocity is not evident or absent.
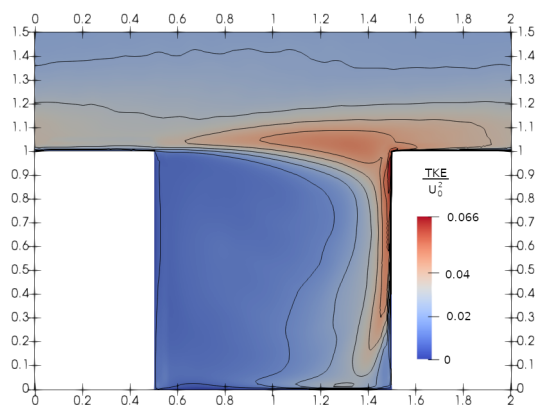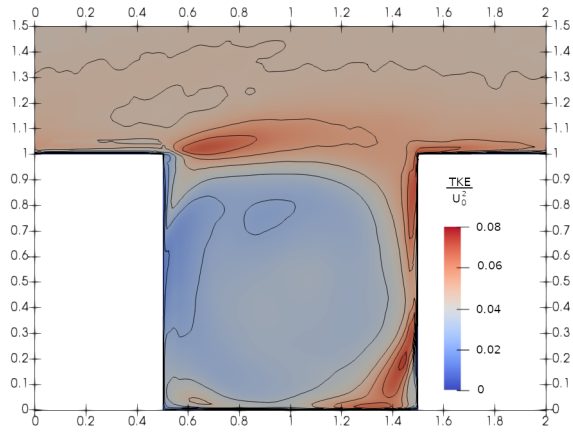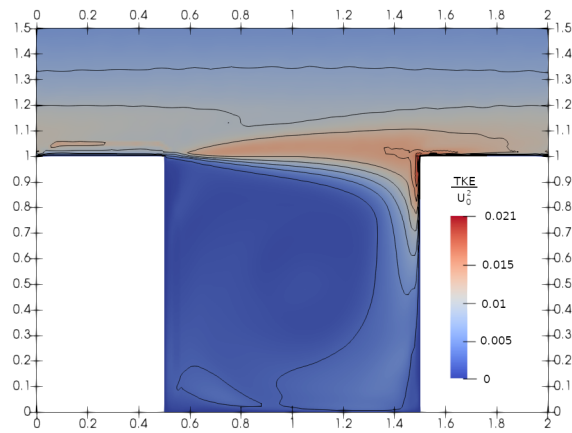
Figure 4.18: Values of the fields of turbulent kinetic energy, from top to bottom: the case withot the channel; the hot channel case; the cold channel case.
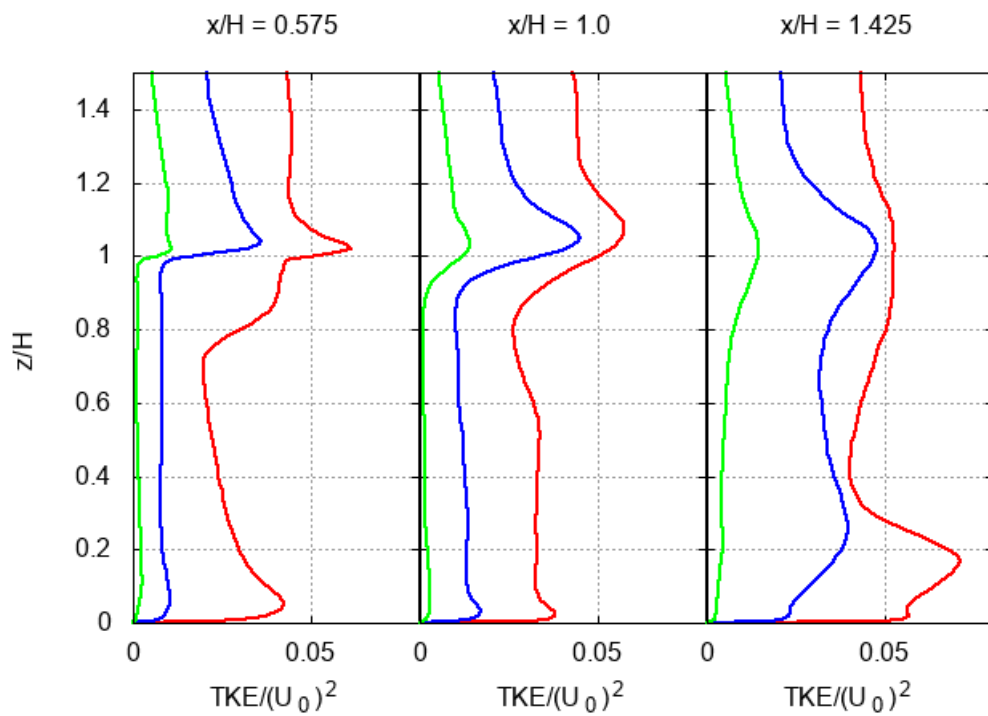
Figure 4.19: Vertical profiles of trbulent kinetic energy for the three cases: without the channel (green lines), hot channel (red lines), cold channel (blue lines); for three different position: near the left wall (left plot), centre of the canyon (middle plot), near the right wall (right plot).

4.3.5 Covariance of horizontal and vertical velocity

Following the turbulent-viscosity hypotheses (for reference see [22]) the covariance of vertical and horizontal velocity may be interpreted as turbulent fluxes of momentum that may be modelled by the gradients of the mean velocity:

$$\langle u'v' \rangle \simeq -\nu_t \left(\frac{\partial \langle u \rangle}{\partial y} + \frac{\partial \langle v \rangle}{\partial x} \right) \tag{4.8}$$

For all the cases, the averaged field will be shown on a vertical section perpendicular to y, and the profiles of temperature along three vertical lines. Each value is adimensionalized dividing by U_0^2.

Figure 4.20 shows the values of covariance of horizontal and vertical velocity. In all the case immidiately over the interface, there are high negative values, in these regions the vertical motion are weak so using eq. (4.8), it may be interpreted as a transmission of horizontal momentum upward, from the main vortex to the region outside the canyon. In the cases with the channel, where the vertical motion is stronger, the peak in the right side is shifted downward at $z/H = 0.1$. The peaks in the bottom right corner and the peak that the hot channel case show in the top left corner are difficult to interpret due to the complex dynamics in that region characterized by a strong gradient in both vertical and horizontal direction and the presence of secondary vortex that affect the motion.

Figure 4.21 displays the covariance of horizontal and vertical velocity for three different value of x/H. The negative peak over the interface is evident in all the profiles. The hot channel case show two positive peaks one in the right profile in the pedestrian region, and the other in the left profile in the interface region. All the features of the profile are stronger in the cases with the channel than the case without it, showing the contribution of vapour concentration in increasing the turbulent fluxes of momentum.
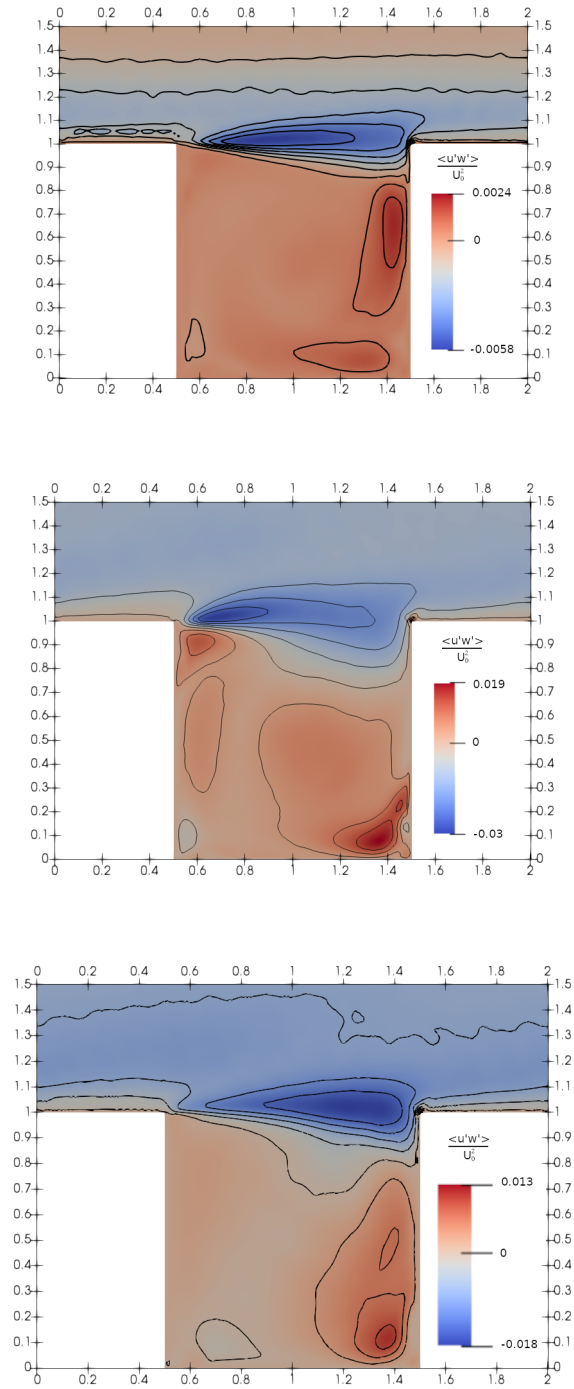
Figure 4.20: Values of the fields of covariances of streamwise and vertical velocities, from top to bottom: the case withot the channel; the hot channel case; the cold channel case.
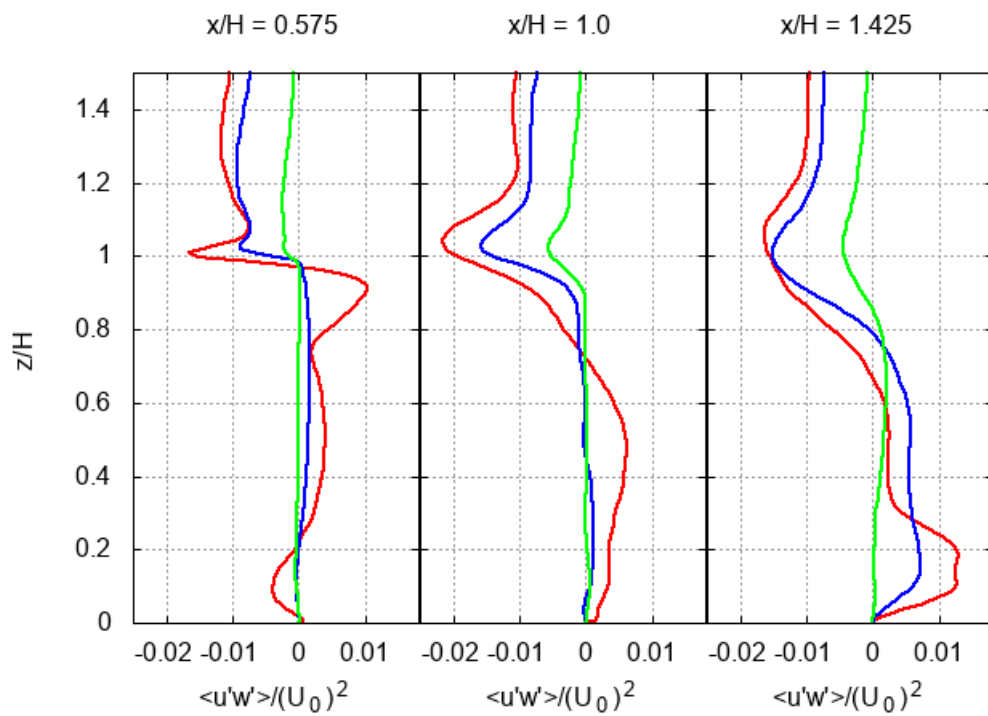
Figure 4.21: Vertical profiles of covariance of streamwise and vertical velocity for the three cases: without the channel (green lines), hot channel (red lines), cold channel (blue lines); for three different position: near the left wall (left plot), centre of the canyon (middle plot), near the right wall (right plot).

4.3.6 Horizontal temperature turbulent fluxes

Following the gradient-diffusion hypothesis (for reference see [22]) the covariance of velocity and a general scalar ϕ may be interpreted as turbulent fluxes of that scalar that may be modelled by the gradients of the mean quantity:

$$\langle u_i'\phi' \rangle \simeq -\alpha_t \left(\frac{\partial \langle \phi \rangle}{\partial x_i} \right) \tag{4.9}$$

This may be used to interpret the temperature fluxes, using T instead of ϕ.

Each value is adimensionalized dividing by $U_0 \Delta T$. Figure 4.22 shows the values of the covariance of horizontal velocity and temperature. The hot channel case does not show any feature except imidiately over the channel and imidiately over the floor at the left side of the channel. In the cold channel case, the regions of negative and positive fluxes over the channel and the floor are more evident. There are also highly positive values over the canyon at $0.6 < x/H < 1.3$.

Figure 4.23 displays the profiles of the covariance of horizontal velocity and temperature. Over the channel, in the central profile, in both cases the fluxes are negative and of similar intensity, which means cold air is transported leftward. In the internal region, the profiles are almost uniform. In the hot channel case near the bottom boundary in the left plot, the profile rapidly changes from negative to positive values, it is difficult to say if it is due to the secondary vortex or to the change in the boundary condition from the channel to the floor. In the cold channel case over the interface, there is a peak of positive value, more intense in central and right profiles, which means that the turbulent fluxes are cooling the region outside the canyon.
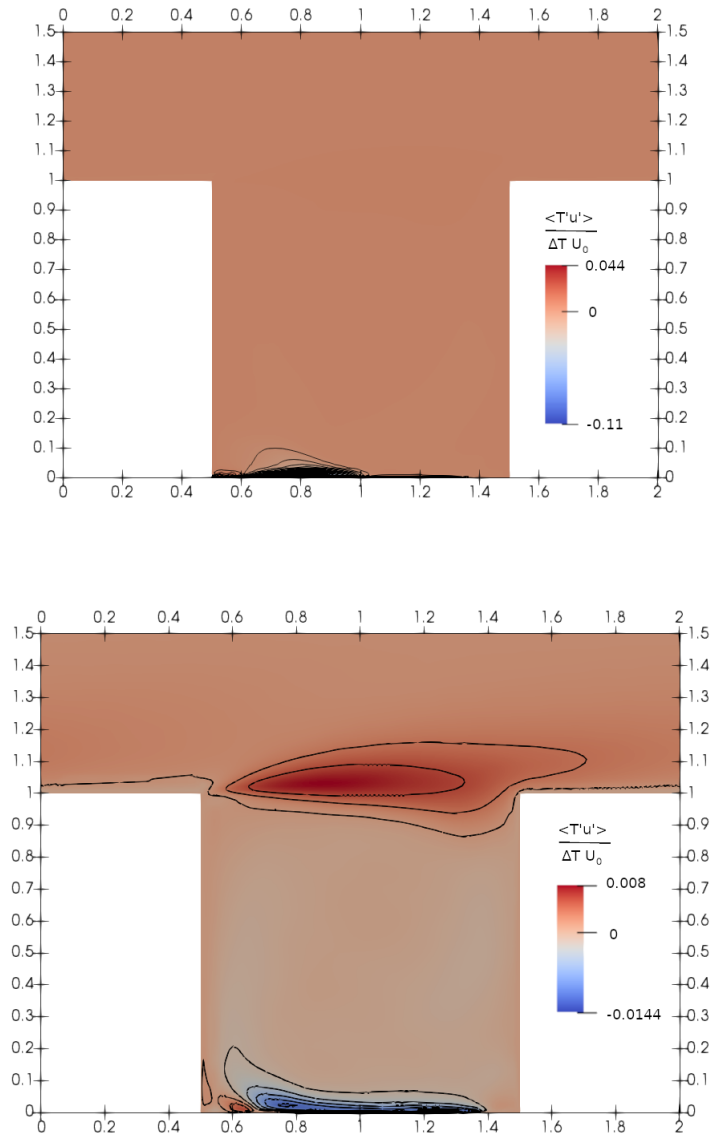
Figure 4.22: Values of the fields of covariances of streamwise velocities and temperatures, of the hot channel case (top), and cold channel case (bottom).
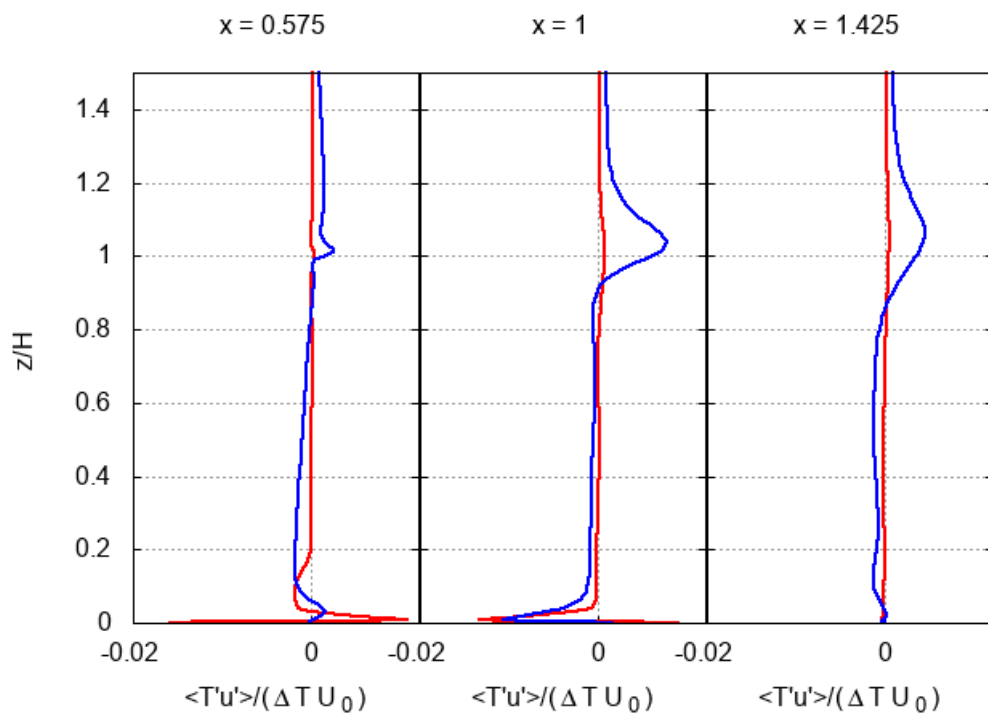
Figure 4.23: Vertical profiles of covariance of streamwise velocity and temperature for the two cases: hot channel (red lines), cold channel (blue lines); for three different position: near the left wall (left plot), centre of the canyon (middle plot), near the right wall (right plot).

4.3.7 Vertical temperature fluxes

The covariance of vertical velocity and temperature will be discussed in this section. Using the eq. (4.9) the vertical turbulent fluxes may be interpretedas a diffusion of temperature along the vertical direction. Each value is adimensionalized dividing by $U_0 \Delta T$.

Figure 4.24 shows the values of covariance of vertical velocity and temperature. In the hot channel case the main gradients are located over the bottom boundary on the left side of the channel, $0.6 < x/H < 0.8$. In the cold channel case, there are negative values over the canyon at $z/H = 1$, so the turbulent fluxes are cooling the outside regions. In the pedestrian region, there are negative values due to the cooling effect of the channel which produces turbulent fluxes that cool the upper air. In the pedestrian region at the corners, $x/H < 0.6$ and $x/H > 1.5$, there are small regions of positive values, in which the air is cooled downward, prossibly related to the corner vortex.

Figure 4.25 shows the profiles of adimensional turbulent vertical thermal fluxes, for three different points of x/H. In the hot channel case, in the central profile, there is a negative peak over the channel at $z/H < 0.1$, that describes the cooling of the upper air from the channel, in the internal regions the fluxes are not appreciable, at $z/H = 1$ there are negative values meaning the turbulent fluxes are cooling upward. In the left profile in the lower pedestrian region, at $z/H < 0.1$ there are high positive values which describe the turbulent fluxes are cooling downward and it is possibly due to the bottom left vortex. In the cold channel case, all the profiles show negative values at $z/H = 1$, meaning that the turbulent fluxes are cooling upward the air outside the canyon. In the internal region, there are negative values in the left and right profiles, so the turbulent fluxes are cooling the air upward. In the pedestrian region in the central profile, there are negative values showing the cooling effect of the channel on the upper air.
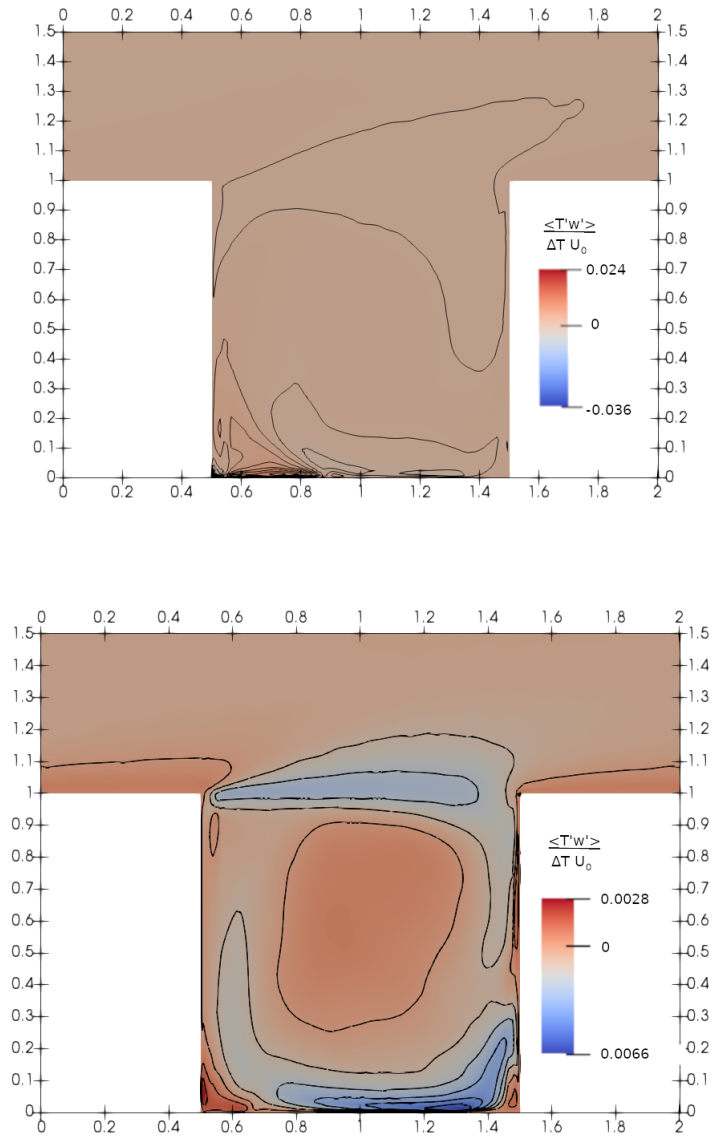
Figure 4.24: Values of the fields of covariances of vertical velocities and temperatures, of the hot channel case (top), and cold channel case (bottom).
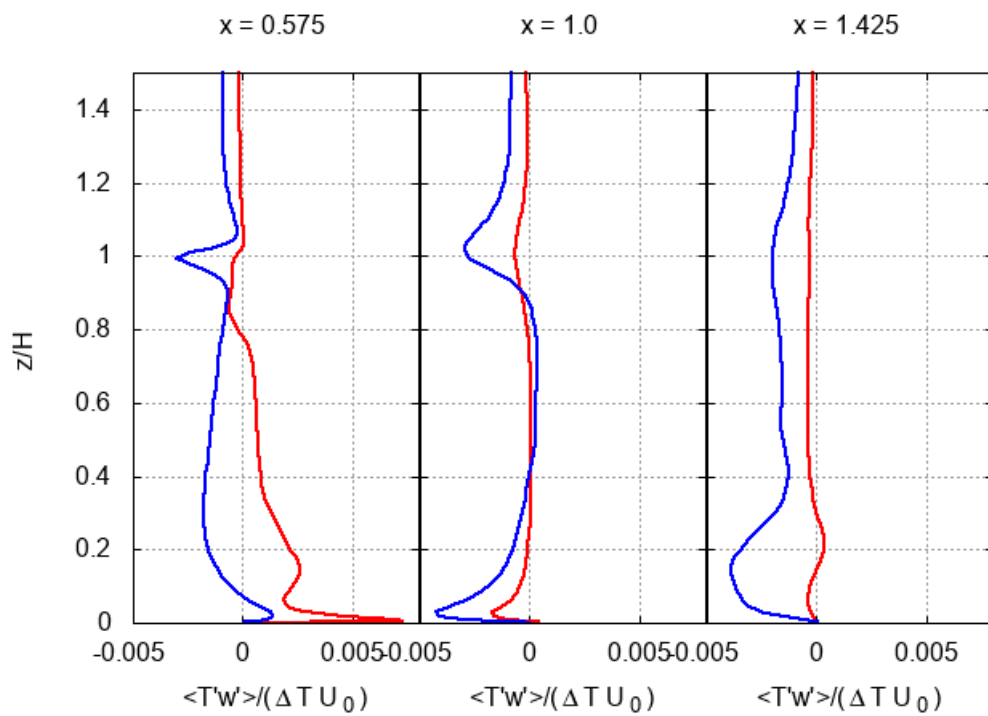
Figure 4.25: Vertical profiles of covariance of vertical velocity and temperature for the two cases: hot channel (red lines), cold channel (blue lines); for three different position: near the left wall (left plot), centre of the canyon (middle plot), near the right wall (right plot).

4.3.8 Horizontal vapour concentration fluxes

Using the eq. (4.9) the horizontal turbulent fluxes may be interpreted as a diffusion of the vapour concentration along the x direction. For all the cases, the averaged field will be shown on a vertical section perpendicular to y, and the profiles of covariance along three vertical lines. Covariance of horizontal velocity and ω is made non-dimensional dividing it by $U_0 \omega_s$.

Figure 4.26 shows the values of turbulent adimensionalized horizontal fluxes. Over the interface, in both cases, there is a region with high negative values, which shows a streamwise transport of humidity into the external region due to the turbulent motions. In both cases, over the channel, there are positive values of turbulent fluxes, which means that humidity is transported leftward. In both bottom corners, in the cold channel case, and the left bottom corners, in the hot channel case, there are small regions of negative values, that may be related to the secondary vortex, in the velocity field.

Figure 4.27 displays the profiles of turbulent adimensional horizontal fluxes of ω for three different values of x/H. In all the profiles are evident the negative peak over the interface, in both cases. In the central profile, there is a positive peak immidiately over the channel, which is more intense in the hot channel case due to the higher evaporation. In both cases, in the lateral profiles, at the bottom of the pedestrian region, there are small negative profiles. In the hot channel case, the left bottom peak is greater than the right one.
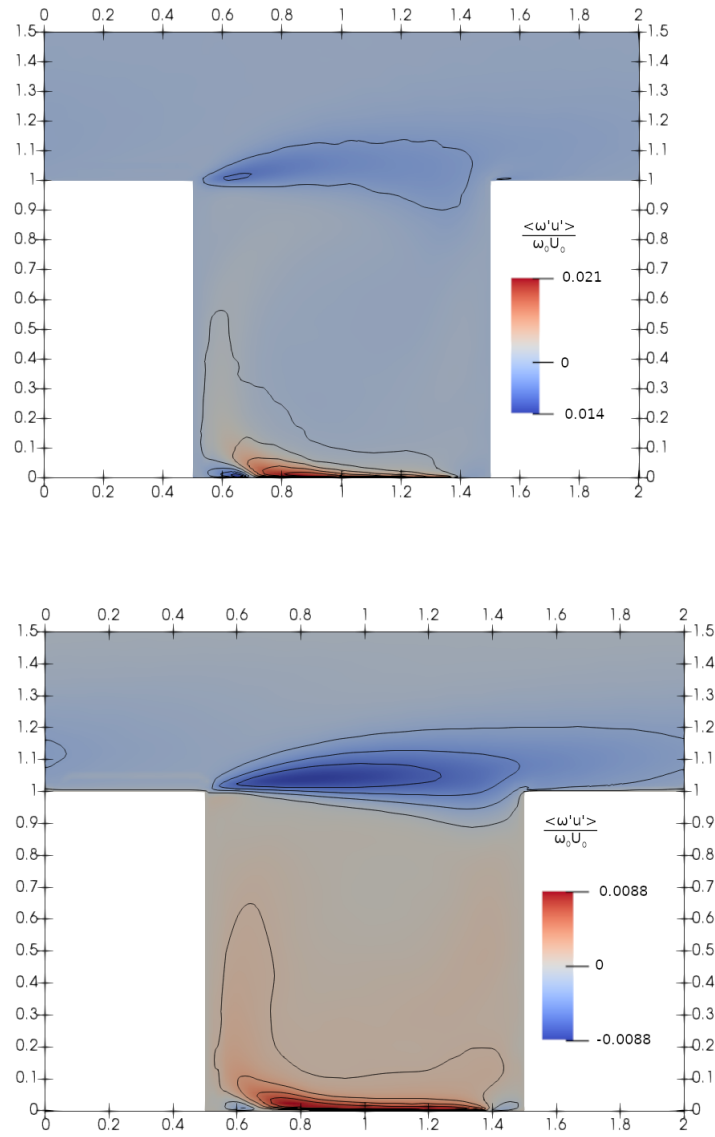
Figure 4.26: Values of the fields of covariances of streamwise velocities and vapour concentrations, of the hot channel case (top), and cold channel case (bottom).
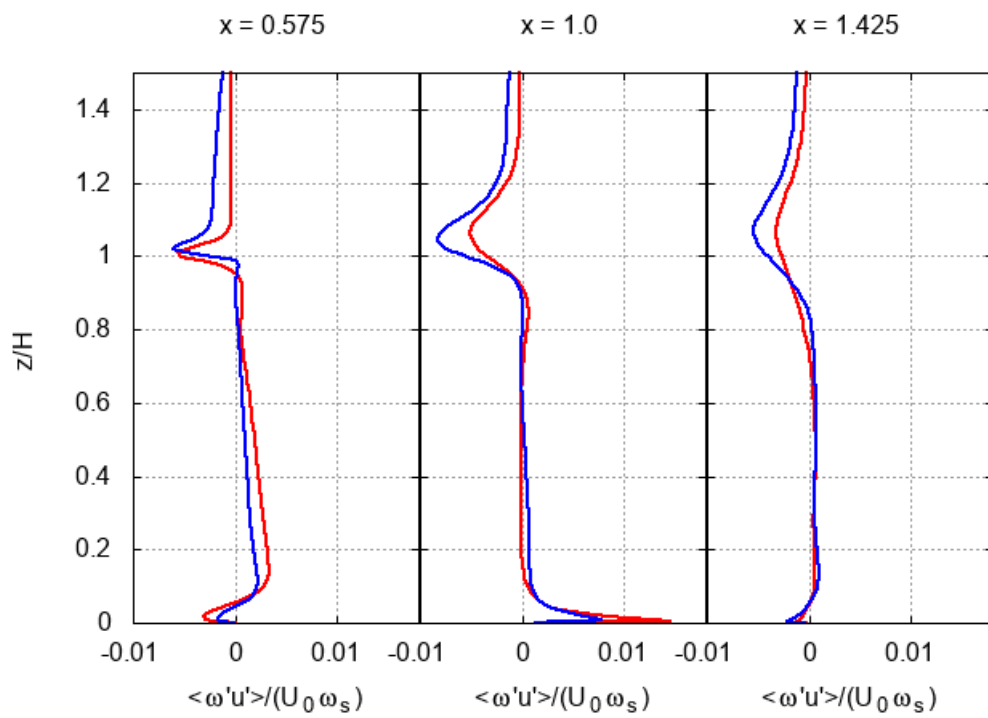
Figure 4.27: Vertical profiles of covariance of streamwise velocity and vapour concentration for the two cases: hot channel (red lines), cold channel (blue lines); for three different position: near the left wall (left plot), centre of the canyon (middle plot), near the right wall (right plot).

4.3.9 Vertical vapour concentration fluxes

The covariance of the vertical velocity component and ω has divided by $U_0\omega_s$ to make it non-dimensional. Using the eq. (4.9) the vertical turbulent fluxes may be interpreted as a diffusion of the vapour concentration along the z direction.

Figure 4.28 shows the values of adimensional turbulent vertical fluxes of ω. In the hot channel case, there are two regions of high positive flux, one over the interface, and the other over the channel spreading along the updraft. In the cold channel case, the regions with the higher fluxes are the region over the interface, and the internal region near the right wall spreading leftward on the downdraft. The positive values are one order of magnitude greater than the negative values, showing that upward diffusion of moisture dominates the entire system.

Figure 4.29 shows the profiles of adimensional turbulent vertical humidity fluxes for three different values of x/H. Near the left wall, both the profiles have positive values all along the canyon, which are greater in the hot channel case. In the central profile, there are two peaks, one at $z/H = 1$ where the humidity is transported to the drier external air, the other over the channel where water evaporates upward. The profiles near the right wall show different behaviour, in the hot channel case, the peak is over the interface, while in the cold channel case the peak is between the internal and pedestrian region.
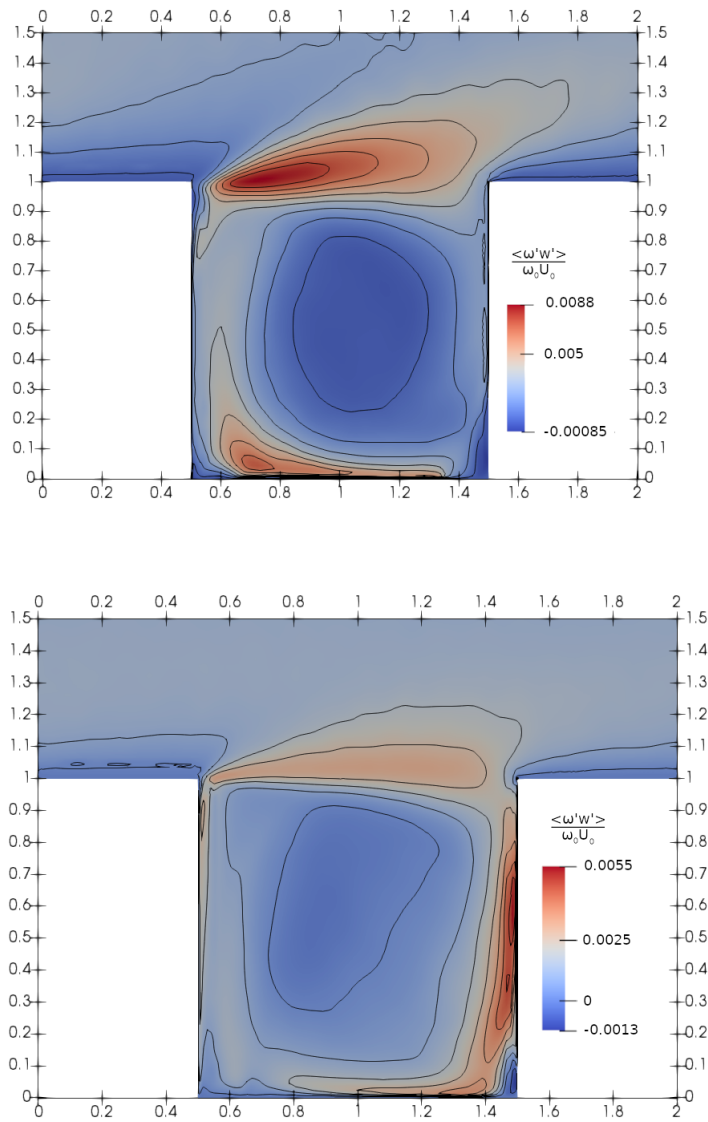
Figure 4.28: Values of the fields of covariances of vertical velocities and vapour concentrations, of the hot channel case (top), and cold channel case (bottom).
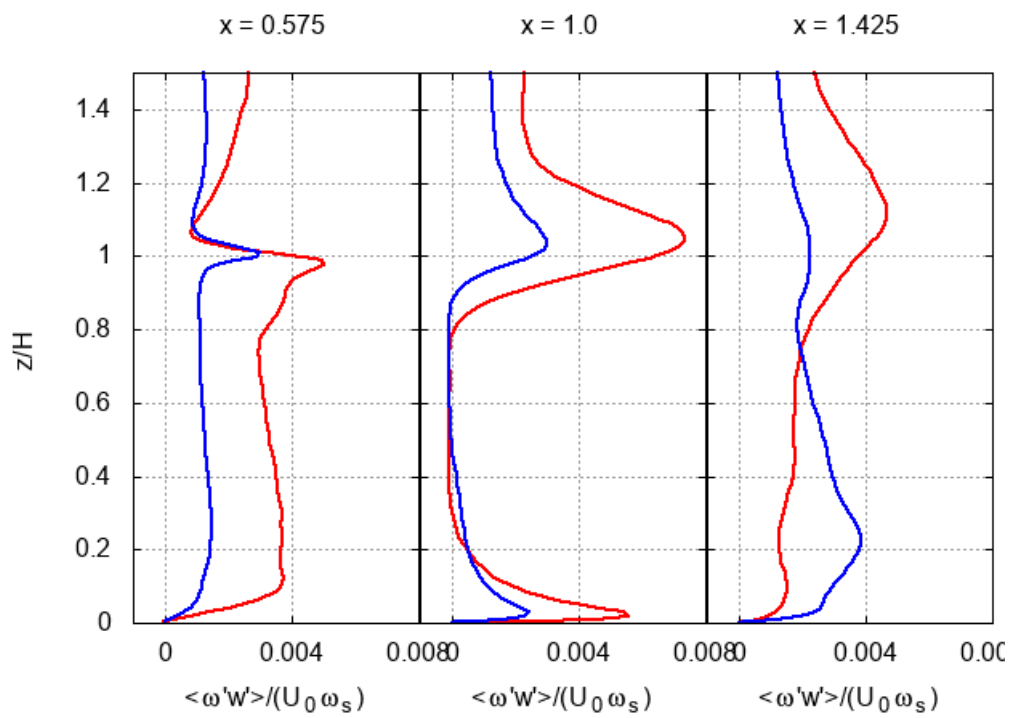
Figure 4.29: Vertical profiles of covariance of vertical velocity and vapour concentration for the two cases: hot channel (red lines), cold channel (blue lines); for three different position: near the left wall (left plot), centre of the canyon (middle plot), near the right wall (right plot).

Chapter 5

Conclusions

The present work has shown the impact of an evaporating waterbody in an urban canyon. This phenomenon has been investigated through numerical simulation using a computational fluid dynamic (CFD) model. A large-eddy simulation (LES) has been chosen as numerical approach, to resolve the evolution of the system by modeling the small scale motions. The model resolves the equations of motion in Boussinesq approximation and the equations of advection and diffusion of temperature and vapour concentration. An evaporation model which describes the evaporation from a water film has been chosen and implemented in the fluid dynamic model. Due to the lack of experimental data to validate the model, it has been tested on a turbulent channel flow with $Re_{tau} = 395$, with different turbulence models. The Smagorinsky model gave the best results and is used in the subsequent simulations. The model is then used in the simulation of an urban street canyon of aspect ratio $H/W = 1$, with H height of the buildings and W width of the street. In the centre of the canyon, an evaporating channel has been placed. Two simulations are performed, with two different channel temperature, one higher than the air temperature and the other lower. The large-eddy simulation approach has permitted to observe the spatial distributions of the mean and turbulent variables.

The results of the simulations show strong interaction between the mechanical and thermodynamical variables. The main vortex developed inside the canyon diffuses the temperature and vapour concentration inside the canyon, and the buoyancy due to the vapour concentration increases the intensity of the vortex. In the hot channel case, the high water temperature has produced high evaporation and so high vapour concentration values in the system. This caused an increase of up to 375% in the horizontal velocity values and up to 300% in the vertical velocity values, these percentages have been computed comparing the maximum velocity values in various regions to the values of the case without the channel In the cold channel case the colder temperature values and lower vapour concentrations have produced weaker effect on the buoyancy, than the previous case, reaching a maximum increase of 130% on the horizontal velocities and of 160% in the vertical velocities. In both cases the presence of the channel has reduced the tem-

perature in the whole domain. In the hot channel case, where the cooling effect of the evaporation opposes the warming effect of thermal diffusion, the temperature reduction was 2-3% of the difference between the channel temperature and the initial air temperature. In the cold channel case, where the cooling effect was greater, the temperature reduction was 10-20% inside the canyon and 7.5% outside. Also the turbulence variables have been changed by the presence of the evaporation. The turbulent kinetic energy in both cases shows higher values than the case without the channel. Turbulent fluxes of momentum show higher values than the case without channel, in particular near the interface between the canyon and the external air, vertical turbulent fluxes of vapour show high values on the left side of the interface. This is particularly interesting because usually, in street canyons, that is a region with high pollutant concentration. So, high turbulence fluxes could contribute to diffuse the pollutant to outside the canyon and reduce the internal concentration.

This work has some limitation due to the model hypothesis used and the simplified setting. The temperature discontinuity on the channel surface may be resolved implementing a model which couples the temperature of the channel to the air temperature. The cold channel case shows the dependence of the buoyancy fields from the boundary conditions of the left building wall, further simulation may study that dependence using different boundary condition and taking in account other physical property of the building facades. The model could be validated using laboratory or scale model data, simulating more complex geometry.

Acknowledgements

Bibliography

[1] AA.VV. User guide - version 6. *The OpenFOAM Foundation*, 10th july 2018.

[2] AA.VV. Programmer's guide - version 3.0.1. *The OpenFOAM Foundation*, 13th December 2015.

[3] AA.VV. World urbanization prospects, the 2018 revisions. *United Nations, Depatment of Economic and Social Affairs*, 2018.

[4] Lup Wai Chew, Amir A. Aliabadi, and Leslie Norford. Flows across high aspect ratio street canyons: Reynolds number independence revisited. *Environmental Fluid Mechanics*, 18:1275–1291, 10 2018.

[5] Carlo Cintolesi, Francesco Barbano, and Silvana Di Sabatino. Large-eddy simulation analyses of heated urban canyon facades. *Energies*, 14(11), 2021.

[6] Carlo Cintolesi, Andrea Petronio, and Vincenzo Armenio. Large-eddy simulation of thin film evaporation and condensation from a hot plate in enclosure: First order statistics. *International Journal of Heat and Mass Transfer*, 101:1123–1137, 10 2016.

[7] Carlo Cintolesi, Andrea Petronio, and Vincenzo Armenio. Large-eddy simulation of thin film evaporation and condensation from a hot plate in enclosure: Second order statistics. *International Journal of Heat and Mass Transfer*, 115, part B:410–423, 12 2017.

[8] Gaëtan Desoutter, Chawki Habchi, Bénédicte Cuenot, and Thierry Poinsot. Dns and modeling of the turbulent boundary layer over an evaporating liquid film. *International Journal of Heat and Mass Transfer*, 52(25):6028–6041, 2009.

[9] Nicoud Franck and Frédéric Ducros. Subgrid-scale stress modelling based on the square of the velocity gradient tensor. *Flow Turbulence and Combustion*, 62:183–200, 09 1999.

[10] E.A. Hathway and S. Sharples. The interaction of rivers and urban form in mitigating the urban heat island effect: A uk case study. *Building and Environment*, 58:14–22, 2012.

[11] Nedyomukti Imam Syafii, Masayuki Ichinose, Eiko Kumakura, Steve Jusuf, Kohei Chigusa, and Nyuk Hien Wong. Thermal environment assessment around bodies of water in urban canyons: A scale model study. *Sustainable Cities and Society*, 34, 06 2017.

[12] R.I Issa. Solution of the implicitly discretised fluid flow equations by operator-splitting. *Journal of Computational Physics*, 62(1):40–65, 1986.

[13] Aytaç Kubilay, Dominique Derome, and Jan Carmeliet. Impact of evaporative cooling due to wetting of urban materials on local thermal comfort in a street canyon. *Sustainable Cities and Society*, 49:101574, 05 2019.

[14] Charles Meneveau, Thomas S. Lund, and William H. Cabot. A lagrangian dynamic subgrid-scale model of turbulence. *Journal of Fluid Mechanics*, 319:353–385, 1996.

[15] H. Montazeri, Y. Toparlar, B. Blocken, and J.L.M. Hensen. Simulating the cooling effects of water spray systems in urban landscapes: A computational fluid dynamics study in rotterdam, the netherlands. *Landscape and Urban Planning*, 159:85–100, 2017.

[16] Robert D. Moser, John Kim, and Nagi N. Mansour. Direct numerical simulation of turbulent channel flow up to re$_\tau$=590. *Physics of Fluids*, 11(4):943–945, 1999.

[17] M. Nunez and T. R. Oke. The energy balance of an urban canyon. *Journal of Applied Meteorology and Climatology*, 16(1):11 – 19, 1977.

[18] T.R. Oke. Street design and urban canopy layer climate. *Energy and Buildings*, 11(1):103–113, 1988.

[19] D. Pearlmutter, E. L. Krüger, and P. Berliner. The role of evaporation in the energy balance of an open-air scaled urban surface. *International Journal of Climatology*, 29(6):911–920, 2009.

[20] Andrea Petronio. Numerical investigation of evaporation and condensation within a tub. 05 2011.

[21] Ugo Piomelli. Large-eddy simulation of turbulent flows. *Department of Mechanical and Materials Engineering, Queen's University, Kingston (Ontario) Canada*, 2018.

[22] Stephen B. Pope. *Turbulent Flows*. Cambridge University Press, 2000.

[23] N. E. Theeuwes, A. Solcerová, and G. J. Steeneveld. Modeling the influence of open water surfaces on the summertime temperature and thermal comfort in the city. *Journal of Geophysical Research: Atmospheres*, 118(16):8881–8896, 2013.

[24] Yoshihide Tominaga, Yuichi Sato, and Satoru Sadohara. Cfd simulations of the effect of evaporative cooling from water bodies in a micro-scale urban environment: Validation and application studies. *Sustainable Cities and Society*, 19, 03 2015.

[25] M. van den Bosch and Å Ode Sang. Urban natural environments as nature-based solutions for improved public health – a systematic review of reviews. *Environmental Research*, 158:373–384, 2017.

[26] H. G. Weller, G. Tabor, H. Jasak, and C. Fureby. A tensorial approach to computational continuum mechanics using object-oriented techniques. *Computers in Physics*, 12(6):620–631, 1998.

[27] Yongling Zhao, Lup Wai Chew, Aytaç Kubilay, and Jan Carmeliet. Isothermal and non-isothermal flow in street canyons: A review from theoretical, experimental and numerical perspectives. *Building and Environment*, 184:107163, 2020.